minerals

MDPI

Article

Mineralization Epochs of Granitic Rare-Metal Pegmatite Deposits in the Songpan–Ganzê Orogenic Belt and Their Implications for Orogeny

Peng Li [1], Jiankang Li [1,*], I-Ming Chou [2], Denghong Wang [1] and Xin Xiong [1]

[1] NRM Key Laboratory of Metallogeny and Mineral Assessment, Institute of Mineral Resources, Chinese Academy of Geological Sciences, Beijing 100037, China; Lipeng031111@163.com (P.L.); wangdenghong@vip.sina.com (D.W.); XiongXin_1989@163.com (X.X.)

[2] CAS Key Laboratory for Experimental Study under Deep-sea Extreme Conditions, Institute of Deep-sea Science and Engineering, Chinese Academy of Sciences, Sanya 572000, China; imchou@idsse.ac.cn

* Correspondence: Li9968@126.com

Received: 15 April 2019; Accepted: 4 May 2019; Published: 7 May 2019

Abstract: Granitic pegmatite deposits, which are usually products of orogenic processes during plate convergence, can be used to demonstrate regional tectonic evolution processes. In the eastern Tibetan Plateau in China, the Jiajika, Dahongliutan, Xuebaoding, Zhawulong, and Ke'eryin rare metal pegmatite deposits are located in the southern, western, northern, midwestern, and central areas of the Songpan–Ganzê orogenic belt, respectively. In this study, we dated two muscovite Ar–Ar ages of 189.4 ± 1.1 Ma and 187.0 ± 1.1 Ma from spodumene pegmatites of the Dahongliutan deposit. We also dated one zircon U-Pb age of 211.6 ± 5.2 Ma from muscovite granite, two muscovite Ar–Ar ages of 179.6 ± 1.0 Ma and 174.3 ± 0.9 Ma, and one columbite–tantalite U-Pb age of 204.5 ± 1.8 Ma from spodumene pegmatites of the Zhawulong deposit. In addition, we dated one muscovite Ar–Ar age of 159.0 ± 1.4 Ma from spodumene pegmatite of the Ke'eryin deposit. Combining these ages and previous studies in chronology, we concluded that the granitic magma in the Jiajika, Xuebaoding, Dahongliutan, Zhawulong, and Ke'eryin deposits intruded into Triassic metaturbidites at approximately 223, 221, 220–217, 212, and 207–205 Ma, respectively, and that the crystallization of the corresponding pegmatite ceased at approximately 199–196, 195–190, 189–187, 180–174, and 159 Ma, respectively. In this study, we demonstrated that the peak in magmatic activity and the final crystallization age of the pegmatite lagged behind one another from the outer areas of the orogeny belt to the inner areas. The pegmatite–parented granitic magmas were sourced from Triassic metaturbidites that were melted by shear heating along the large-scale decollement resulting from Indosinian collisions along the North China block, Qiangtang–Changdu block, and Yangtze block. As a result, the above temporal and spatial regularities indicated that the tectonic–thermal stress resulting from the collisions of three blocks was transferred from the outer areas of the orogenic belt to the inner areas. A large amount of heat and a slow cooling rate at the convergent center of thermal stress in two directions will lead to crystallization and differentiation of magma in the Songpan–Ganzê orogenic belt, forming additional rare metal deposits.

Keywords: granitic pegmatite; rare metal deposit; Mesozoic mineralization; Songpan–Ganzê orogenic belt; orogenic process

1. Introduction

Li-Cs-Ta (LCT) [1] pegmatites are sources of strategic metals [2]. They are usually orogenic products of magmatic activity [1,3] occurring in the plate convergence process [4,5]. As a result, the evolution of global pegmatites, from their inception and peak to their decline and eventual

extinction, is associated with changes in the tectonics of the lithosphere [6]. In addition, the main peaks in the LCT pegmatite age distribution are generally consistent with the epochs of supercontinent assembly [4]. For example, the occurrence peaks of LCT-type pegmatite from 2368 Ma, 1800 Ma, 962 Ma, 529–485 Ma, and 371–274 Ma coincide with the assemblies of Sclavia and Superia, Nuna, Rodinia, Gondwana, and Pangea, respectively [4]. Therefore, pegmatites and pegmatite-type rare metal deposits are used to trace tectonic history, particularly continental orogenic processes.

For example, through regional pegmatite, Pedrosa et al. [7] studied the opening of the South Atlantic, and Galetskiy [8] and Mints [9] discussed the tectonic evolution of the Eastern Baltic and Ukrainian shields, respectively. Mohammedyasin et al. [10] claimed that the rare metal mineralization of the Kenticha deposit in southern Ethiopia marked the end of the East African Orogeny, and Makrygina et al. [11] concluded that the Ol'khon rare metal pegmatoid granites marked the beginning of the Hercynian within-plate stage in the eastern Baikal area of Russia.

The Songpan–Ganzê orogenic belt, located in the eastern Tibetan Plateau, is one of the most important granitic pegmatite mineralization belts in China [12]. It has a complex tectonic history as a result of the interactions between three major continental blocks (North China, Yangtze, and Qiangtang–Changdu) during the closure of the Paleo-Tethys in the Late Triassic [13,14]. In this tectonic setting, widespread granitic pegmatite-type rare metal deposits were formed [15]. Although a number of studies regarding the ages of regional pegmatite and related granitic intrusions have been published to date [16–19], there has not been a systemic summary of the regional diagenesis and mineralization process. By supplementing several essential dating results, in this paper we systematically summarize the spatiotemporal distribution of rare metal pegmatite deposits in the Songpan–Ganzê orogenic belt. In addition, we estimate the cooling rate and time of different pegmatite ore fields according to the closure temperatures of different isotope dating systems. Based on the results, we investigate the implications of these pegmatite-type deposits for orogeny in the Songpan–Ganzê orogenic belt.

2. Regional Geological Features

The Songpan–Ganzê orogenic belt is in contact with the Yangtze, North China, and Qiangtang–Changdu blocks along the Longmenshan thrust-nappe belt [20], Miaulue-A'nyemaqen suture [21], and Jinsha suture, respectively (Figure 1). In the Songpan–Ganzê orogenic belt, Sinian strata are distributed along the eastern edge of the belt. Triassic flysch sediments, composed primarily of sandstone and slate, are distributed in the main section of the belt with a thickness of more than 10,000 m [22]. The flysch sediments have undergone metamorphism to different degrees, resulting in serial medium-pressure metamorphic domed bodies, including the Yajiang, Ke'eryin, Zhawulong, and Zhibosong domes. Usually, pegmatite dikes and their parental granites intrude into the core of these metamorphic domes; however, Indosinian tectonic movement shortened the crust as a result of the collision of the Yangtze, Qiangtang–Changdu, and North China blocks [15].

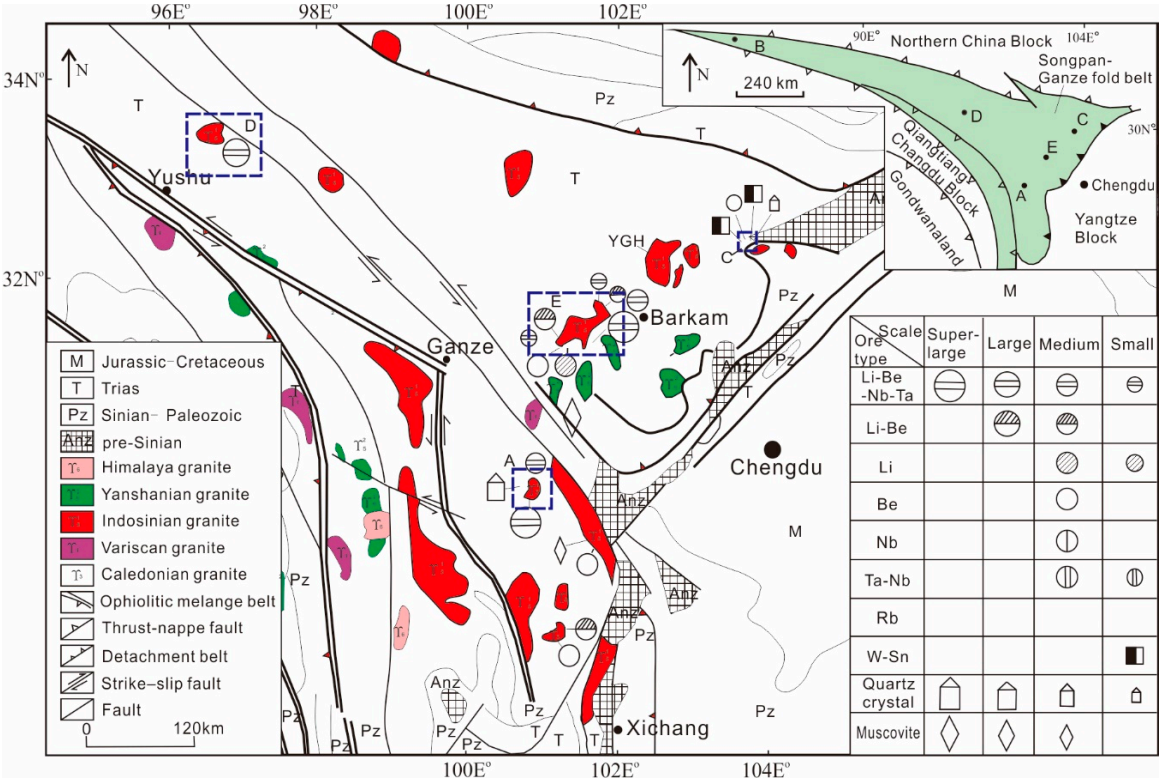

Figure 1. Distribution map of granitic pegmatite deposits in the western Sichuan Province, China. A: Jiajika Li–Be–Nb–Ta pegmatite deposit; B: Dahongliutan Li–Be–Nb–Ta pegmatite deposit; C: Xuebaoding W–Sn pegmatite deposit; D: Zhawulong Li–Be–Nb–Ta pegmatite deposit; E: Ke'eryin Li–Be–Nb–Ta pegmatite deposit; YGH: Yanggonghai granite.

In the metamorphic domes of the Songpan–Ganzê orogenic belt, granitic pegmatite deposits occur around granitic intrusions and contain abundant rare metal resources (Figure 1), including lithium. The Jiajiaka, Dahongliutan, and Ke'eryin rare metal deposits are also super-large lithium deposits, containing Li_2O reserves of more than 2,000,000, 3,000,0000, and 2,000,000 tons, respectively [12,23–26]. The Xuebaoding deposit is famous worldwide for its infrequent platy beryl crystals and integral scheelite crystals [27], and the Zhawulong deposits may potentially be super-large rare metal deposits [28]. In addition, these granitic pegmatite deposits contain high-grade rare metal elements of more than 1.2 wt.% Li_2O at shallow burial depth.

3. Geological Features of Major Pegmatite Deposits

3.1. Jiajika Li–Be–Ta–Nb Deposit

The Jiajika pegmatite deposit, located in the southern Songpan–Ganzê orogenic belt (location A; Figure 1), is hosted in the Yajiang metamorphic dome. In the Jiajika pegmatite field, pegmatite dikes surround the granite body both horizontally and vertically (Figure 2). The wall rocks of the two-mica granite and pegmatites are composed of mudstone and sandstone from the Late Triassic period. The main tectonic features controlling ore distribution are joints and fissures that formed before or during pegmatite emplacement. The rocks that contain the Jiajika granite underwent multistage metamorphism during magmatism, leading to the development of five distinct metamorphic zones that surround the granite; from the inner zones to the outer zones, these are the diopside, staurolite, andalusite–staurolite, andalusite, and biotite zones. The total area of the metamorphic zones is approximately 500 km^2 [27].

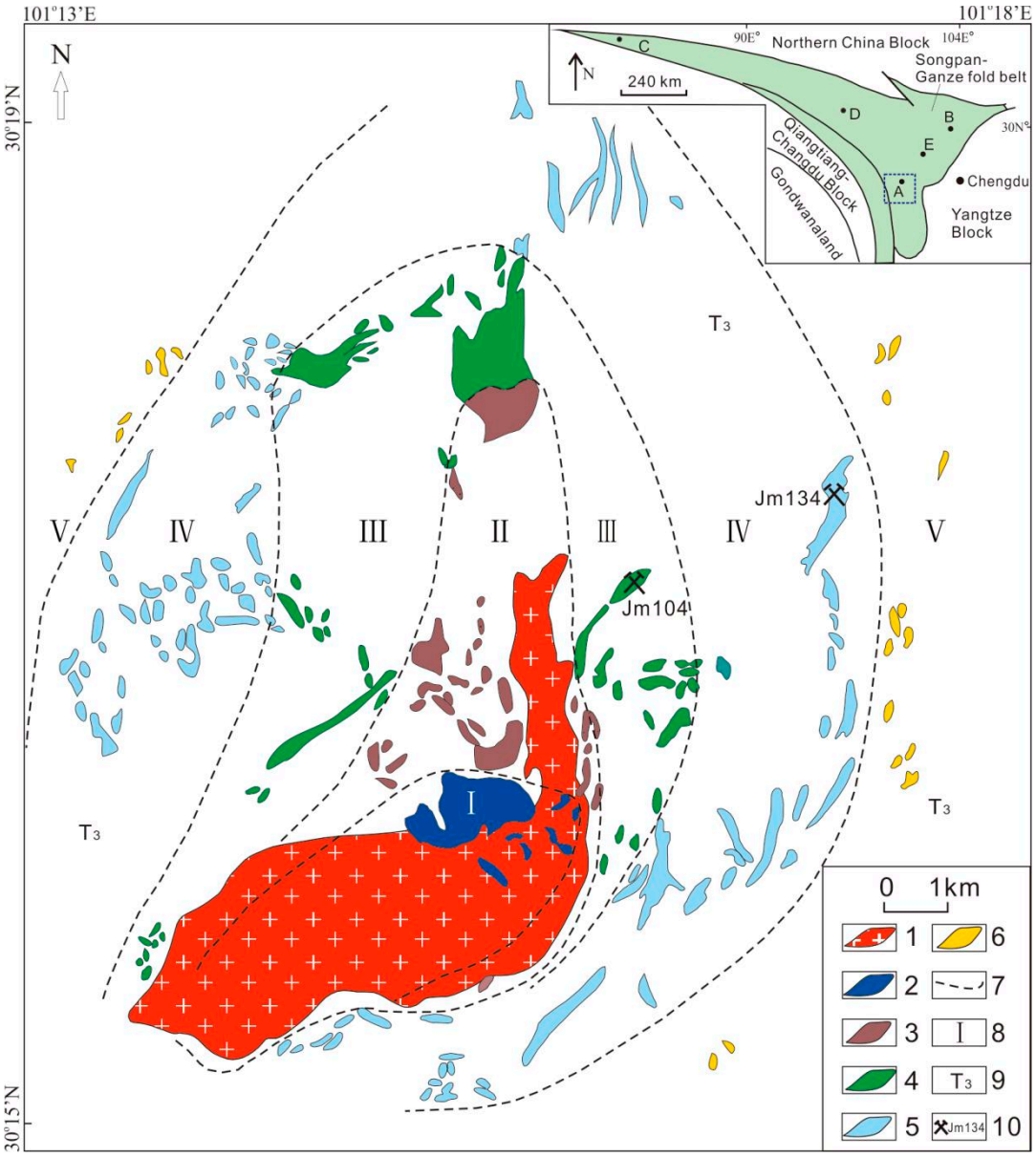

Figure 2. Distribution map of granitic pegmatites in the Jiajika Li–Be–Nb–Ta deposit, Sichuan Province, China. 1: Two-mica granite; 2: Microcline pegmatite; 3: Microcline–albite pegmatite; 4: Albite pegmatite; 5: Albite–spodumene pegmatite; 6: Lepidolite (muscovite) pegmatite; 7: Zoning lines of different types of pegmatite; 8: Zone number of different pegmatite types. I: Microcline pegmatite zone; II: Microcline–albite pegmatite zone; III: Albite pegmatite zone; IV: Spodumene pegmatite zone; V: Lepidolite (muscovite) pegmatite zone; 9: Upper Triassic sandstone and mudstone; 10: Muscovite sampling location with sample number in Table 1. The legend for the diagram in the upper right-hand corner is provided in Figure 1.

In the Jiajika deposit, a total of 498 pegmatite dikes with a length × width of more than 20 m^2 are distributed in an area of approximately 80 km^2. On the basis of mineral paragenetic associations, each pegmatite dike can be divided into three to five mineral zones. On the basis of the main mineral zones, the pegmatite dikes can be classified into five types: microcline pegmatite (I), microcline–albite pegmatite (II), albite pegmatite (III), spodumene pegmatite (IV), and lepidolite (muscovite) pegmatite (V; Figure 2). Farther away from the type-V pegmatite zone, many quartz veins are present. The major minerals in the pegmatite dikes are microcline, albite, quartz, and muscovite. These coexist with rare

metal-element-bearing minerals, such as spodumene, titanium samarskite, beryl, thorite, cyrtolite, cymatolite, and sicklerite, as well as volatile-bearing minerals, such as tourmaline and fluorite [27].

3.2. Dahongliutan Li–Be–Nb–Ta Deposit

The Dahongliutan pegmatite deposit is located in the western area of the Songpan–Ganzê orogenic belt (location B; Figure 1). In the Dahongliutan ore field, more than 110 pegmatite dikes occur in an outcrop area of approximately 31.5 km^2 surrounding the Yanshanian two-mica granite (Figure 3). Irregular schlieren pegmatite dikes occur within the granite. In addition, in the middle Proterozoic biotite schist and sillimanite–andalusite–biotite–quartz schist, muscovite–microcline, muscovite–microcline–albite, and spodumene pegmatite dikes occur proximally to distally from the granite in that order. The spodumene pegmatite dikes, including dikes No. 90, 91, 93, 102, and 104, are composed primarily of an albite–spodumene zone and quartz–spodumene zone with several albite–lepidolite aggregations. The lithium oxide (Li_2O) reserves of five spodumene pegmatite dikes are greater than 50,000 t and have a Li_2O content of 1.24–1.62% [23].

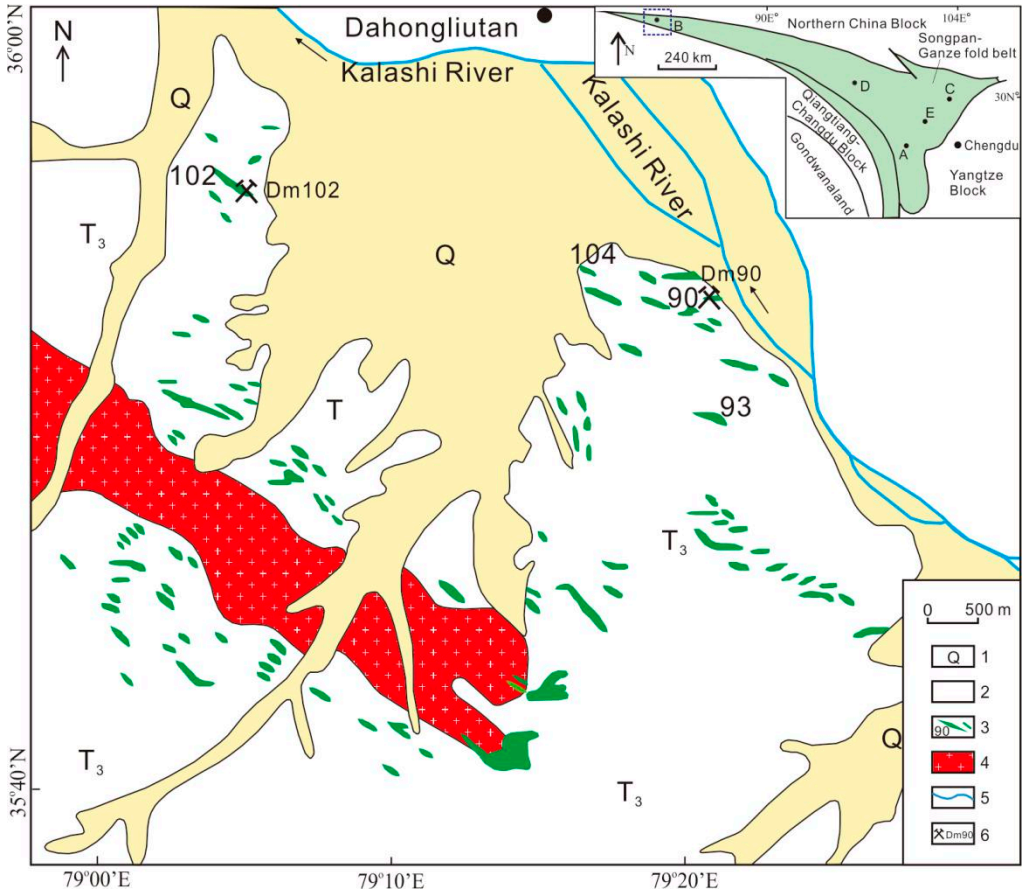

Figure 3. Geological map of the Dahongliutan Li–Be–Nb–Ta deposit in Xinjiang, China. 1: Quaternary sediment; 2: Upper Triassic biotite schist and sillimanite–andalusite–biotite–quartz schist; 3: Pegmatite dikes with numbers; 4: Two-mica granite; 5: Stratigraphic boundary; 6: Muscovite sampling location with sample number in Table 1. The legend for the diagram in the upper right-hand corner is provided in Figure 1.

3.3. Xuebaoding W–Sn–Be Deposit

The Xuebaoding granitic pegmatite deposit, located in the northern area of the Songpan–Ganzê orogenic belt (location C; Figure 1), is hosted in the Zhibosong metamorphic dome. In the ore field, the Pankou and Pukou muscovite plagiogranites intruded into the Middle Triassic strata composed of

sericite–quartz phyllite, under the control of the dome core (Figure 4). The Pukou and Pankou granitic intrusions contain cassiterite, scheelite, chalcopyrite, galena, sphalerite, molybdenite, and pyrite with clear zonal structures of marginal, transitional, and core zones. Fissures in the Triassic wall rock provided pathways and precipitation sites for pegmatite-forming fluid exsolved from granitic magma. Most mineralized pegmatite dikes occur, as a group, between the Pankou and Pukou granite (Figure 4). The main metal minerals in pegmatite dikes are scheelite, cassiterite with other metallic sulfides, quartz, muscovite, fluorite, feldspar, and beryl. Scheelites, which are normally present in the outer sections of pegmatite dikes, are often white or pale yellow cubic-bipyramidal crystals, some of which weigh up to 1 kg. Beryl crystals are short hexagonal prisms, white or light green in color, and can weigh up to 1 kg [29].

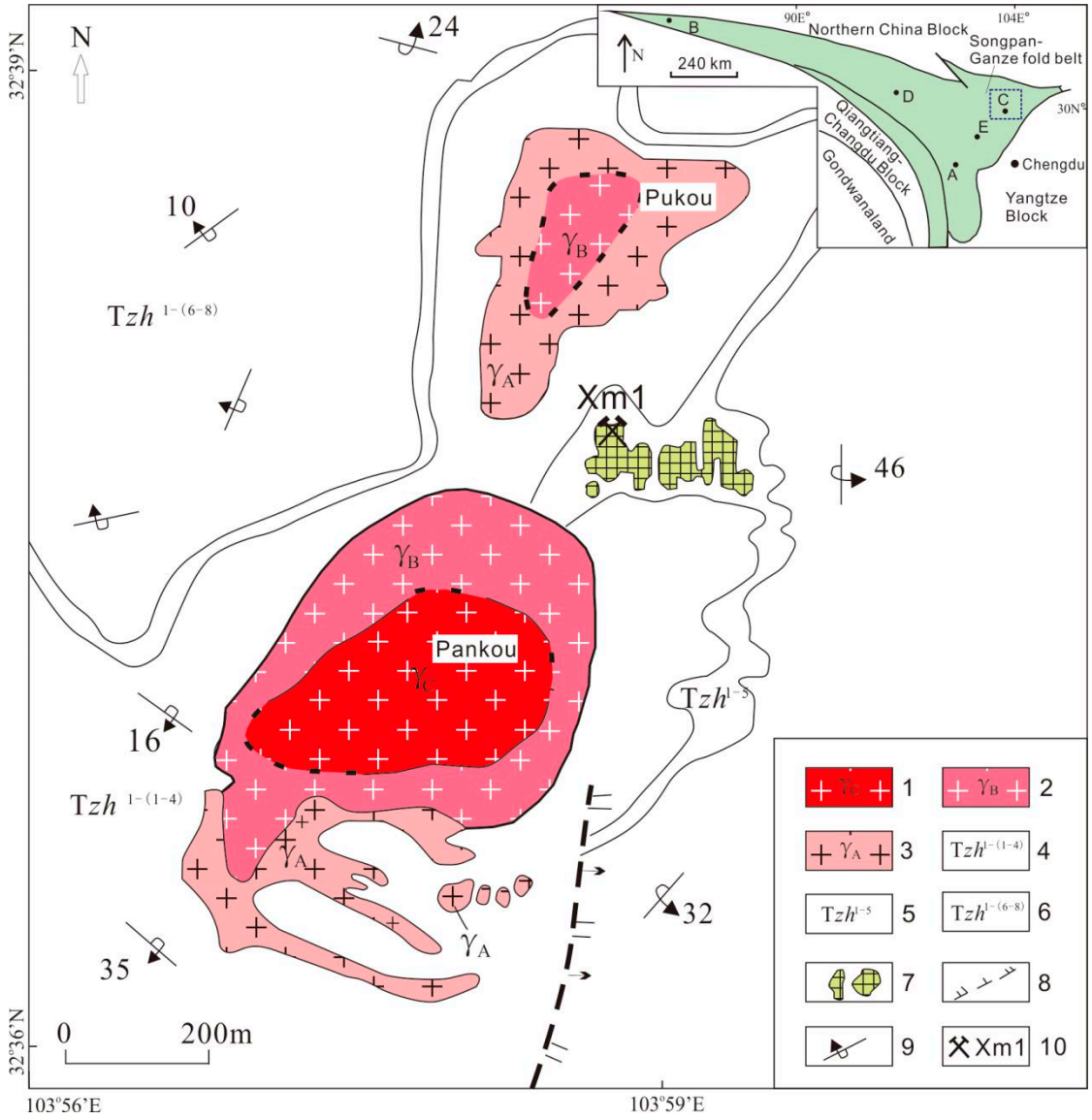

Figure 4. Geological map of the Xuebaoding granitic pegmatite W–Sn deposit, Sichuan Province, China. 1: Marginal zone of granite; 2: Middle zone of granite; 3: Core zone of granite; 4: Quartz schist, marble, and biotite quartz schist of the Triassic Zhuwo Formation; 5: Marble-bearing mineralization pegmatite dikes of the Triassic Zhuwo Formation; 6: Calcium quartz schist and sericite–quartz schist of the Triassic Zhuwo Formation; 7: Area of mineralization pegmatite dikes; 8: Inferred fault; 9: Attitude of strata; 10: Muscovite sampling location with sample number in Table 1. The legend for the diagram in the upper right-hand corner is provided in Figure 1.

The Yanggonghai intrusion is also located in the northern area of the Songpan–Ganzê orogenic belt. It is located approximately 100 km west of the Xuebaoding deposit, with outcrop areas of 980 km^2 (Figure 1) [27]. The granite intruded into the Late Triassic sandstone. In addition, many mineralization-barren granitic pegmatite dikes are present within the granitic intrusions and their wall rocks. This granite-pegmatite system is similar to the Xuebaoding deposit, although it has undergone strong erosion [27].

3.4. Zhawulong Li–Be–Ta–Nb Deposit

The Zhawulong pegmatite deposit is located in the midwestern areas of the Songpan–Ganzê orogenic belt (location D; Figure 1). The Quaternary coverage of the ore field is greater than 50%, and the outcropped strata are Triassic mudstone and sandstone. The Zhawulong muscovite granite, which is the metallogenic parent rock of the rare metal deposit, intruded into Triassic mudstone and sandstone (Figure 1) along the Zhawulong anticline, occurring as an irregular fusiform intrusion with an outcrop area of 58 km^2. The residual roof of wall rock still remains at the top of the granitic intrusion, indicating a low degree of regional denudation.

In the ore field, 111 pegmatites are mainly distributed around the contact zone of the Zhawulong granitic intrusion and the Triassic sediments; 36% of them show mineralization of rare metals (Figure 5). More than 20 pegmatites demonstrate significant mineralization with Li_2O content ranging from 1.2% to 1.5%. Among them, pegmatite No. 14 has the largest Li mineralization scale, with a surface outcropping extension of approximately 2000 m and a thickness of approximately 5 m. The entire vein is mineralized with an average Li_2O grade of 1.2% and Li_2O reserves of 100,000 tons, while the Li_2O reserves of the Zhawulong deposit are approximately 160,000 tons, approaching the scale of large lithium deposits [28].

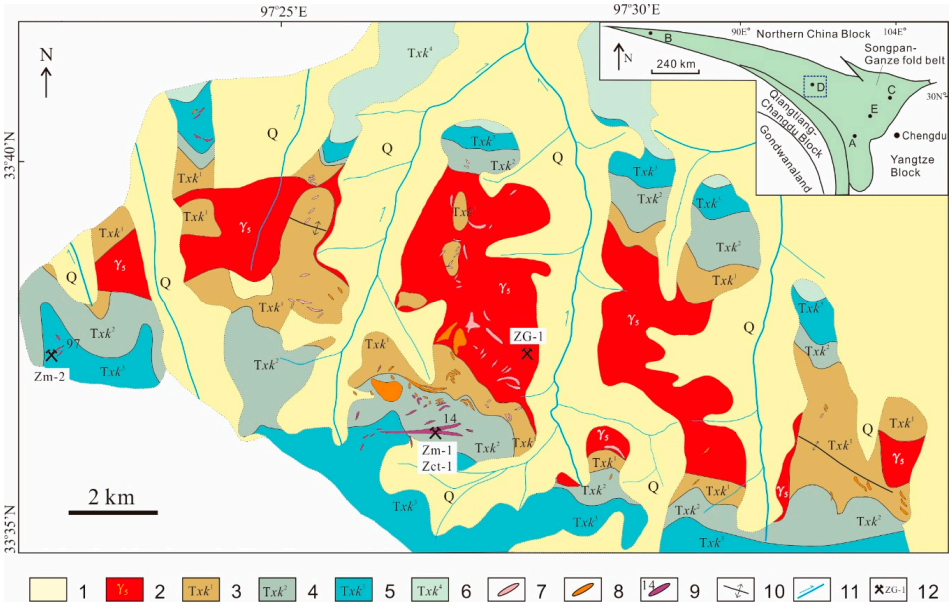

Figure 5. Geological map of the Zhawulong Li–Be–Nb–Ta deposit in Xinjiang, China. 1: Quaternary sediment; 2: Muscovite granite; 3: Biotite quartz quartzite and biotite granulite with transgranular pyroxene kernels; 4: Biotite quartz (staurolite or andalusite) schist; 5: Biotite granulite, biotite quartz schist; 6: Phyllite rock metamorphism sandstone and metamorphic shale; 7: Microcline pegmatite; 8: Microcline feldspar pegmatite; 9: Albite–spodumene pegmatite and number; 10: Anticline axis; 11: River and flow direction; 12: Sampling location with sample number in Table 1. The legend for the diagram in the upper right-hand corner is provided in Figure 1.

3.5. Ke'eryin Li–Be–Ta–Nb Deposit

The Ke'eryin pegmatite deposit is located in the central area of the Songpan–Ganzê orogenic belt (location E; Figure 1). In the ore field, a complex granitic intrusion, composed of a series of medium-acidity magmatic rocks, intruded into the Triassic sandstone during the late Indosinian period. Two-mica granite, with an outcrop area of 188 km^2, dominates this intrusion that was controlled by the axial lobe of the Ke'eryin anticline (Figure 6). On the basis of the intrusion and incision relationships, the granitic intrusion formed in a full fractional crystallization process that produced quartz diorite, biotite granite, biotite adamellite, biotite K-feldspar granite, two-mica granite, and muscovite–albite granite in turn [27]. Similarly to the metamorphic belt in the Jiajika deposit, the pyroxene–hornfels facies, amphibolite–hornfels facies, albite–epidote–hornfels facies, andalusite belt, staurolite–grossularite belt, and biotite belt surround the complex granitic intrusions.

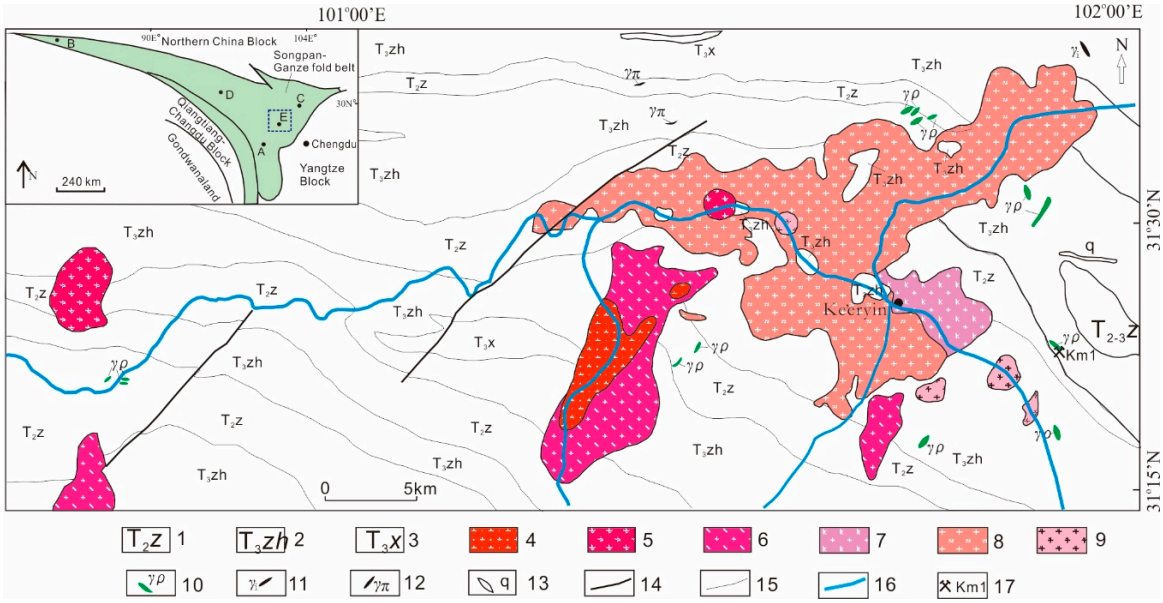

Figure 6. Geological map of the Ke'eryin rare metal deposit in Sichuan Province, China. 1: Quartz sandstone and slate of the Middle Triassic Zaguniao Formation; 2: Sandstone of the Upper Triassic Zhuwo Formation; 3: Sericite slate of the Upper Triassic Xindu Formation; 4: Quartz diorite; 5: Biotite granite; 6: Biotite adamellite; 7: Biotite K-feldspar granite; 8: Two-mica granite; 9: Muscovite–albite granite; 10: Pegmatite dike; 11: Granitic aplite vein; 12: Granitic porphyry vein; 13: Quartz dike; 14: Fault; 15: Stratigraphic boundary; 16: River; 17: Muscovite sampling location with sample number in Table 1. The legend for the diagram in the upper left-hand corner is provided in Figure 1.

In the Ke'eryin ore field, approximately 548 mineralized pegmatite dikes, including 263 spodumene pegmatite dikes, have been discovered [30]. These pegmatite dikes are 50–300 m in length and 2–10 m in thickness. They occur in groups around the complex granitic intrusion. The Ke'eryin ore field contains six main types of dikes: two-mica microcline, muscovite–microcline, muscovite–microcline–albite, muscovite–albite, muscovite–albite–spodumene, and muscovite–albite–lepidolite. The first four types are mineralization-barren pegmatite dikes that mainly occur within granite, and the second two types are rare metal pegmatites that mainly occur in Triassic sandstones. The Ke'eryin ore field produced two super-large lithium deposits (Li_2O reserves ≥500,000 tons)—the Dangba and Lijiagou deposits and several medium-large lithium deposits. The Dangba large-scale pegmatite dikes of muscovite–albite–spodumene with massive reserves are located primarily in the southeastern area of the ore field. The main rare metal minerals found in the Ke'eryin pegmatite are spodumene, beryl, columbite–tantalite minerals, and cassiterite [30]. The potential reserves of Li_2O in this region may be greater than 7,000,000 tons [25].

4. Sampling and Dating Methods

In this study, the muscovite samples used for Ar–Ar dating were extracted from the spodumene pegmatites of the Dahongliutan, Zhawulong, and Ke'eryin ore fields, and the zircon and columbite–tantalite samples used for U-Pb dating were extracted from the Zhawulong ore field. Muscovite samples Dm90 and Dm102 were sampled from spodumene pegmatite dikes No. 90 and No. 102 in the Dahongliutan deposit, respectively (Figure 3). Dm90 and Dm102 were white in color, shaped as large sheets, and coexisted with quartz, albite, and spodumene (Figure 7a,b).

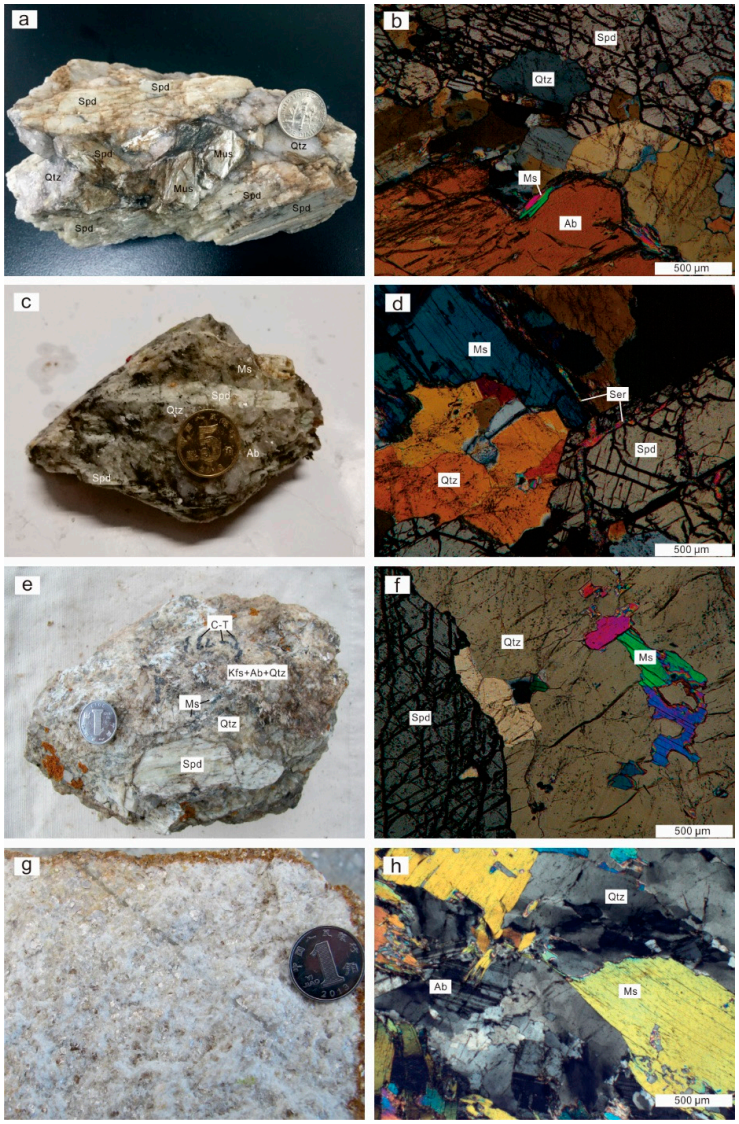

Figure 7. Hand specimen (left) and thin section (right) photographs illustrating sample structure, grain size, and major mineral assemblages of pegmatites and granite. Qtz: quartz; Ms: muscovite; Ab: albite; Kfs: K-feldspar; Spd: spodumene; C–T: columbite–tantalite. (**a**,**b**) Dahongliutan spodumene pegmatite; (**c**,**d**) Ke'eryin spodumene pegmatite; (**e**,**f**) Zhawulong spodumene pegmatite; (**g**,**h**) Zhawulong muscovite granite.

In the Ke'eryin ore field, muscovite sample Km1 was sampled from the Dangba spodumene pegmatites (Figure 6). Km1 was white in color and shaped as fine sheets with straight quartz and feldspar boundaries (Figure 7c,d). In the Zhawulong ore field, muscovite samples Zm-1 and Zm-2 were sampled from the spodumene pegmatite dikes No. 14 and No. 97, respectively (Figure 5). Zm-1 and Zm-2 were white in color, shaped as large sheets, and coexisted with quartz, albite, and spodumene

(Figure 7e,f). Zircon samples ZG-1 were sampled from fresh muscovite granite in the southeast part of the Zhawulong granite (Figure 7g,h). The columbite–tantalite samples of Zct-1 were sampled from the No. 14 spodumene pegmatite dikes. Most were shaped as hypidiomorphic long or short columns and coexisted with quartz, albite, and spodumene (Figure 7e).

Due to the large sheets, the fresh muscovite samples of Dm90 and Dm102 from the Dahongliutan ore field were removed by hand. These individual muscovite crystals were then cut into chips ≤0.15 mm in size prior to cleaning in an ultrasonic bath. The Km1 muscovite samples were separated from spodumene pegmatite samples weighing approximately 6 kg. The samples were crushed, and grains <0.5 mm were separated by sieving, with >99% pure fresh muscovite removed by hand using a binocular microscope. Zm-1 and Zm-2 were separated from two spodumene pegmatite samples. They were then crushed, and grains <0.5 mm were separated by sieving, with >99% pure fresh muscovite removed by hand using a binocular microscope.

During Ar–Ar dating, muscovite samples were sealed in a quartz ampoule that was irradiated for 1440 minutes in the nuclear reactor (The Swimming Pool Reactor, Chinese Institute of Atomic Energy, Beijing). The reactor delivers a neutron flux of ~2.60×10^{13} n·cm^{-2} s^{-1}; The integrated neutron flux is about 2.25×10^{18} n·cm^{-2}. The monitor irradiated together with the samples is an internal standard: Fangshan biotite (ZBH-25) whose age is 132.7 Ma and its potassium content is 7.6% [31]. Following irradiation, the samples were incrementally heated to release argon in the extremely high-vacuum argon extraction system at the Laboratory of Ar–Ar Isotopic Dating, Institute of Geology, Chinese Academy of Geological Sciences in Beijing, China. The purified argon extracted during heating was analyzed by Mass Spectrometer GV Helix MC (GV Instruments, Ltd; Manchester, UK).

Apparent ages for each heating stage were corrected for mass discrimination, atmospheric Ar concentration, blank values, and interfering isotopes, and ^{37}Ar values were corrected for radioactive decay. The correction factors for interfering isotopes produced during irradiation used in this study were as follows: $(^{36}Ar/^{37}Ar)_{Ca} = 2.40 \times 10^{-4}$, $(^{40}Ar/^{39}Ar)_{K} = 47.82 \times 10^{-4}$, and $(^{39}Ar/^{37}Ar)_{Ca} = 8.06 \times 10^{-4}$. The ^{40}K decay constant used for analysis was $\lambda = 5.543 \times 10^{-10}$ a^{-1}, with an age error of 1 σ. The entire analytical procedure used for the Ar–Ar analysis was identical to the one outlined in Chen and Zhang (2002) [32].

Zircon separation and cathodoluminescence (CL) imaging were performed at the Beijing SHRIMP Center at the Chinese Academy of Geological Sciences. Zircon grains were extracted from rock samples using conventional procedures of rock crushing, sieving, elutriating, drying, dressing by magnetic separation, electromagnetic selection, heavy liquid separation, and handpicking under a binocular microscope. Zircon grains were then mounted onto double-sided adhesive tape and enclosed in a 2.5-cm-diameter epoxy resin disk. The morphology of the zircon crystals was examined in both transmitted and reflected light, and images were captured using an optical microscope and a CL imaging system. The procedures were identical to those described in Liu et al. (2015) [33].

Zircon U–Pb dating analysis was performed via LA-ICP-MS at the National Research Center of Geoanalysis in Beijing, China. Laser sampling was performed using an ESI New Wave 193 laser ablation system (Electro-Sensors, Inc.; Hopkins, MN, USA). Ion signal intensities were detected with a Thermo ELMENT XR instrument (Thermo fisher scientific; Waltham, MA USA). Helium was used as a carrier gas and argon as the make-up gas; the two gases were mixed via a T-connector prior to entering the ICP. Each analysis incorporated background acquisition for approximately 20 s (gas blank) followed by 40 s of data acquisition from the sample. The ICPMSDataCal(11.4) software was used to perform off-line raw data selection, integration of background and analytical signals, and time-drift correction and quantitative calibration for U–Pb dating [34]. Common Pb was corrected according to the method proposed in [35].

For the analysis, we used a spot size of 23 μm, and time-dependent elemental fractionation was minimized by using a laser frequency of 8 Hz. Zircon GJ-1 (601.0 ± 1.7 Ma, 2σ, [36]) was used as an external standard for U–Pb dating and was analyzed twice every 10 analyses. Time-dependent drifts of U–Th–Pb isotopic ratios were corrected using linear interpolation (with time) for every 10 analyses

according to variations detected in GJ-1. The uncertainty in the preferred values (0.5%) for the external standard GJ-1 was propagated to the final results of the samples. Common Pb correction was found to be unnecessary for the analyzed zircons due to a low signal from common ^{204}Pb and a high ^{206}Pb/^{204}Pb ratio. The U, Th, and Pb concentrations were calibrated on the basis of glass standard NIST SRM 612 which was produced by National Institute of Standards and Technology (NIST, USA) to ensure that the ^{232}Th and ^{238}U signals were greater than 20 MeV. The oxide yield was controlled to less than 0.2%, and the isotope signal ratio of ^{238}U/^{232}Th was controlled to approximately 1 by monitoring the ThO^+/Th^+ ratio. The Isoplot/Ex_ver3 tool was used to construct concordia diagrams and calculate weighted means. Plešovice zircons were dated as unknown samples and yielded a weighted mean ^{206}Pb/^{238}U age of 337 ± 2 Ma (2SD, n = 12), which is in good agreement with the standard ^{206}Pb/^{238}U age of 337.13 ± 0.37 Ma (2SD) [37]. Determining the ages of zircons (>1000 Ma) must be based primarily on their ^{207}Pb/^{206}Pb ages. The zircon ^{206}Pb/^{238}U ages were reported at a 1σ uncertainty level.

The analytical procedures used for columbite–tantalite U–Pb dating are described in detail in Che et al. (2015) [38]; a brief overview is provided below. U–Pb dating was performed using a Resolution S-155 193-nm excimer ArF laser ablation system coupled to a Thermo Fisher Scientific iCAP-Q quadrupole inductively coupled plasma mass spectrometer (Q-ICP-MS) at the State Key Laboratory for Mineral Deposits Research at Nanjing University, China. During analysis, the laser was set to a fluence of approximately 7.5 J/cm^3, a spot size of 67 μm, and a repetition rate of 4 Hz. Each group of five unknowns was bracketed by the analysis of two zircon standards (91500 and GJ-1) and one columbite–tantalite reference material (Coltan 139). Each analysis consisted of approximately 30 s of background acquisition, 60 s of data acquisition with the laser running, and up to 60 s to flush the system. The external columbite–tantalite reference standard and data processing method were identical to those described in [38]. The ^{206}Pb/^{238}U ages were reported at a 1σ uncertainty level.

5. Results

5.1. Muscovite ^{40}Ar/^{39}Ar Dating

In the Dahongliutan ore field, step heating and ^{40}Ar/^{39}Ar analyses of Dm90 yielded a flat age spectrum for heating steps between 800° and 1400° C, with a well-defined plateau age of 187.0 ± 1.1 Ma, for 99.34% of the ^{39}Ar released during analysis (Table A1 and Figure 8). The inverse isochron age of ^{36}Ar/^{40}Ar versus ^{39}Ar/^{40}Ar is 187.2 ± 1.9 Ma, with an initial ^{40}Ar/^{36}Ar ratio of 301 ± 13 (mean square weighted deviation (MSWD) = 27), approximating modern atmospheric Ar values (295.5 ± 5; Figure 8; [39]). The muscovite sample Dm102 yielded a flat age spectrum for heating steps between 760° and 1400° C, with a well-defined plateau age of 189.4 ± 1.1 Ma, for 99.77% of the ^{39}Ar released during analysis (Table A1 and Figure 8). The inverse isochron age of ^{36}Ar/^{40}Ar versus ^{39}Ar/^{40}Ar is 188.0 ± 2.0 Ma, with an initial ^{40}Ar/^{36}Ar ratio of 305 ± 23 (MSWD = 57).

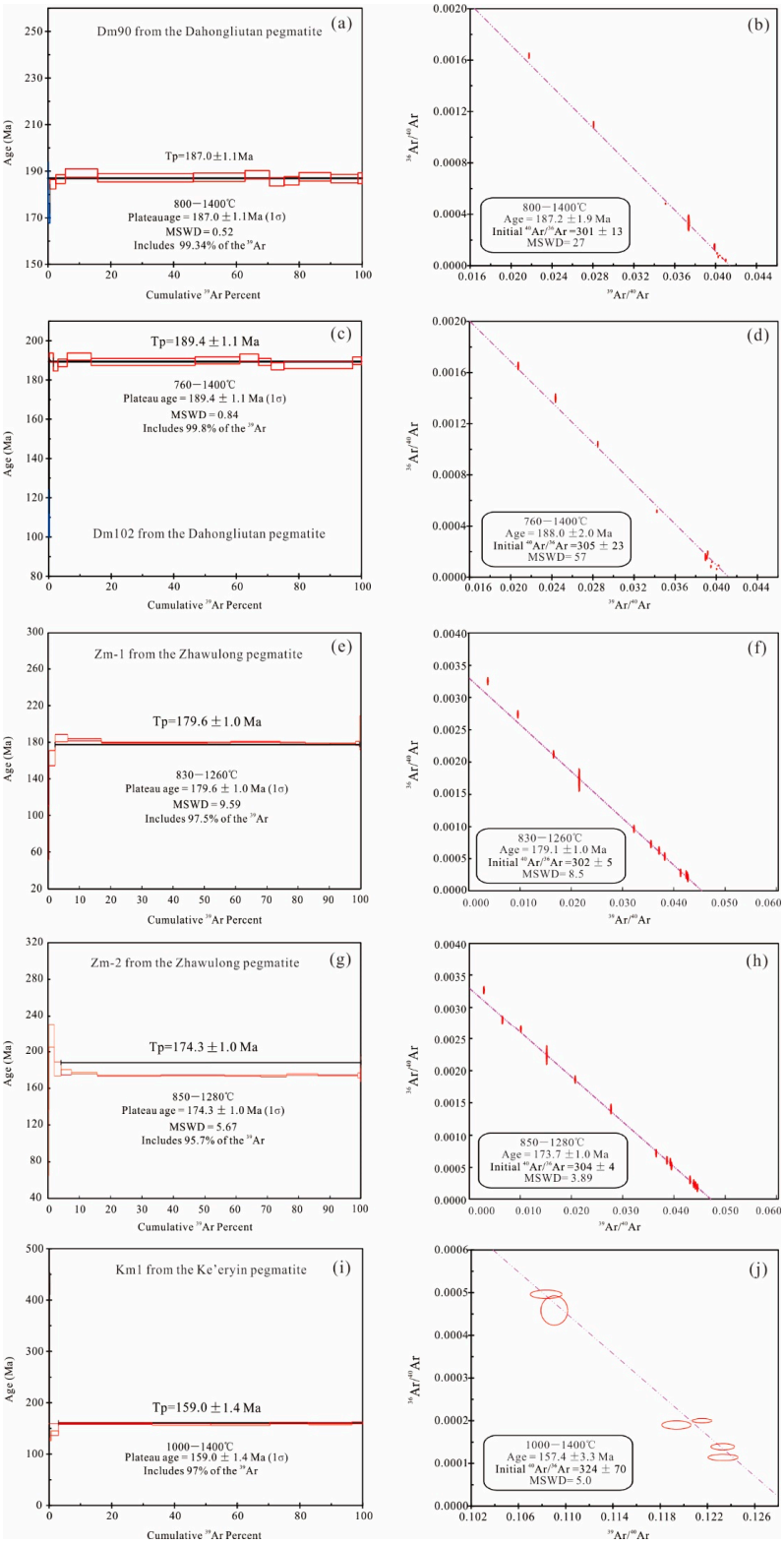

Figure 8. $^{40}Ar/^{39}Ar$ plateau age spectra (left) and inverse isochron age spectra (right) for muscovite samples from the pegmatite dikes of the Dahongliutan, Zhawulong, and Ke'eryin deposits in the Songpan–Ganzê orogenic belt. (**a**–**d**) $^{40}Ar/^{39}Ar$ plateau age spectra (left) and inverse isochron age spectra (right) for muscovite samples from the Dahongliutan pegmatites; (**e**–**h**) $^{40}Ar/^{39}Ar$ plateau age spectra (left) and inverse isochron age spectra (right) for muscovite samples from the Zhawulong pegmatites; (**i**,**j**) $^{40}Ar/^{39}Ar$ plateau age spectra (left) and inverse isochron age spectra (right) for muscovite samples from the Ke'eryin pegmatite.

In the Zhawulong ore field, step heating and $^{40}Ar/^{39}Ar$ analyses of Zm-1 yielded a flat age spectrum for heating steps between 830 and 1260 °C, with a well-defined plateau age of 179.6 ± 1.0 Ma, for 97.5% of the ^{39}Ar released during analysis (Table A1 and Figure 8). The inverse isochron age of $^{36}Ar/^{40}Ar$ versus $^{39}Ar/^{40}Ar$ is 179.1 ± 1.0 Ma, with an initial $^{40}Ar/^{36}Ar$ ratio of 302 ± 5 (MSWD = 8.5), approximating modern atmospheric Ar values (295.5 ± 5; Figure 8; [39]). The muscovite sample Zm-2 yielded a flat age spectrum for heating steps between 850° and 1280° C, with a well-defined plateau age of 174.3 ± 0.9 Ma, for 95.7% of the ^{39}Ar released during analysis (Table A1 and Figure 8). The inverse isochron age of $^{36}Ar/^{40}Ar$ versus $^{39}Ar/^{40}Ar$ is 173.7 ± 0.9 Ma, with an initial $^{40}Ar/^{36}Ar$ ratio of 304 ± 4 (MSWD = 3.89).

In the Ke'eryin deposit, step heating and $^{40}Ar/^{39}Ar$ analyses for Km1 yielded a flat age spectrum for heating steps between 1000° and 1400° C, with a well-defined plateau age of 159.0 ± 1.4 Ma, for 97% of the ^{39}Ar released during analysis (Table A1 and Figure 8). In the $^{36}Ar/^{40}Ar$ versus $^{39}Ar/^{40}Ar$ inverse isochron diagram, the muscovite analyses yielded an age of 157.4 ± 3.3 Ma, with an initial $^{40}Ar/^{36}Ar$ ratio of 324 ± 70 (MSWD = 5.0), approximating modern atmospheric Ar values (295.5 ± 5; Figure 8; [39]).

These results indicate that the $^{40}Ar/^{39}Ar$ isotope system in muscovite samples, extracted from the pegmatite dikes in the Dahongliutan, Zhawulong, and Ke'eryin deposits, remained closed and was not affected by the presence of excess argon or argon loss after crystallization.

5.2. Zircon U–Pb Dating

The CL images of zircons captured from the Zhawulong granite are presented in Figure 9. The zircons are either hypidiomorphic or idiomorphic, and most are composed of a magmatic core with relatively obvious oscillatory zoning and a narrow metamorphic overgrowth rim with obscure zoning. These metamorphic overgrowth rims may have been recrystallized during late metamorphism and causes the decrease of the Th/U ratio of zircon [40,41]. All 28 spots have Th/U ratios of 0.01–3.18, and 25 of them are between 0.04 and 1.85. The zircon U–Pb dating results are provided in Table A2. The majority of the analyses are concordant, and the discordant spots reveal the characteristics of $^{207}Pb/^{206}Pb > {}^{207}Pb/^{235}$ U $> {}^{206}Pb/^{238}$ U (e.g., spots 7, 8, 13, 16, 18), which indicate various degrees of radiogenic lead loss.

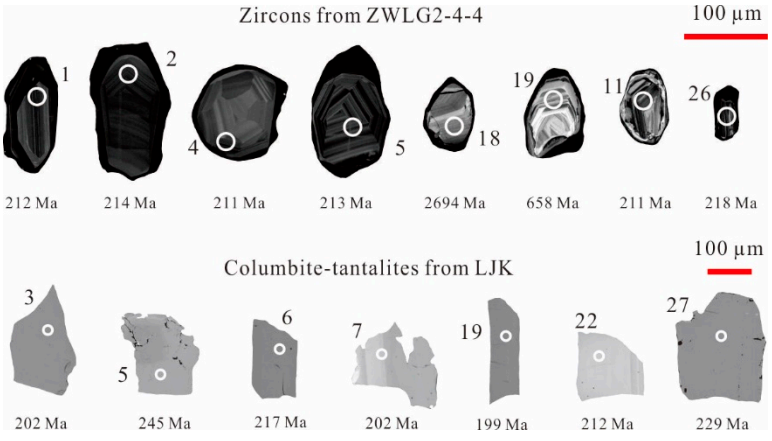

Figure 9. Cathodoluminescence images of representative zircons and columbite–tantalites from the Zhawulong deposit. White circles indicate the analytical spots that provide the measured ages below each image.

Because the overgrowth rims were too narrow for measurement (<10 μm), 28 spot analyses were performed on the magmatic core of 28 zircon grains from ZG-1. A total of 14 spots deviated significantly from the concordia, and the remaining 14 spots yielded a weighted mean $^{206}Pb/^{238}U$ age of 211.6 ± 5.2 Ma (1σ, MSWD = 0.15, n = 14) (Figure 10).

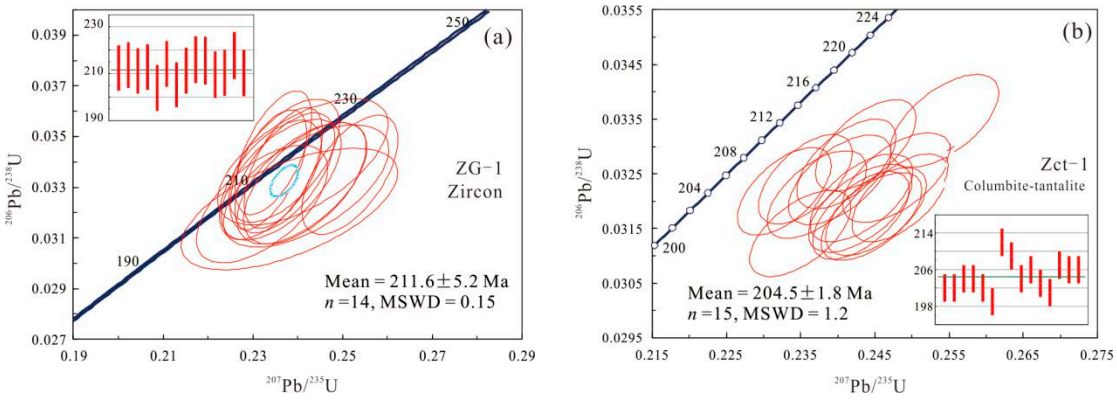

Figure 10. U–Pb concordia diagrams for samples from the Zhawulong deposit (acquired using LA-ICP-MS). (**a**) U–Pb concordia diagram for zircons from the Zhawulong granite; (**b**) U–Pb concordia diagram for columbite–tantalites from the Zhawulong pegmatite.

5.3. Columbite–Tantalite U–Pb Dating

The CL images of the columbite–tantalites captured from the Zhawulong No. 14 spodumene pegmatite dike are presented in Figure 9. Most of the columbite–tantalite grains were shaped as subhedral long or short columns, and several grains displayed weak oscillation zones. The U-Pb isotopic compositions of the columbite–tantalite grains were measured using spot analysis. All data obtained are provided in Table A2, and the calculated ages are plotted in Figure 10.

Forty spot analyses were performed on 40 columbite–tantalite grains from Zct-1. A total of 25 spots deviated significantly from the concordia due to the influence of inclusions (e.g., spot 7, 12, 13, and 17) or high concentrations of common Pb associated with cracks. A total of 15 spots yielded a weighted mean $^{206}Pb/^{238}U$ age of 204.5 ± 1.8 Ma (1σ, MSWD = 1.2, n = 15).

6. Discussion

6.1. Ages of Pegmatite Deposits in the Songpan–Ganzê Orogenic Belt

The dating data presented in this paper provide reliable temporal constraints for the magmatic activities related to rare metal mineralization in the Songpan–Ganzê orogenic belt. The spodumene pegmatites of the Ke'eryin ore field produced muscovite Ar–Ar age of 159.0 ± 1.4 Ma, while the spodumene pegmatites in the Dahongliutan ore field produced muscovite Ar–Ar ages of 189.4 ± 1.1 Ma and 187.0 ± 1.1 Ma. In addition, the muscovite Ar–Ar ages of spodumene pegmatites in Zhawulong ore field were 179.6 ± 1.0 Ma and 174.3 ± 0.9 Ma. The zircon concordant age of 211.6 ± 5.2 Ma for the Zhawulong muscovite granite is interpreted to be its emplacement age, which is close to the columbite-tantalite U-Pb age of 204.5 ± 1.8 Ma of the spodumene pegmatites in the Zhawulong ore field.

In addition to the dating results obtained in this study, many other muscovite Ar–Ar ages, zircon U–Pb ages, and columbite–tantalite U–Pb ages of pegmatites in western Sichuan have been reported. The sampling locations and dating results are listed in Table 1. The dating results for the main granitic intrusions related to regional pegmatite deposits, including those in the Yanggonhai, Jiajika, Ke'eryin, and Dahongliutan granitic intrusions, are also summarized in Table 1.

The geochronological analyses summarized in Table 1 indicate that different isotope systems provide different ages, mainly due to the different closure temperatures for these isotopic systems in different minerals [42] rather than the crystallization order of the minerals. In granitic magma, the closure temperatures for the U–Pb system in zircon is 800–900 °C [43–46]. This is consistent with the granitic magma temperature, and therefore the U–Pb age of zircon can be regarded as the granite emplacement age.

Table 1. Dating results for pegmatite deposits and granitic intrusions in the Songpan–Ganzê orogenic belt. Numbered locations of samples are provided in Figures 2–6.

Location	Sampling Locations (Muscovite Sample Number)	Dating Method	Age (Ma)	References
Jiajika ore field	Two-mica granite	Zircon U–Pb	223 ± 1	Hao et al. [16]
	No. 3 spodumene pegmatite dike	Columbite–tantalite U-Pb	214 ± 2	Hao et al. [16]
	No.104 spodumene pegmatite dike (Jm104)	Muscovite Ar–Ar	196 ± 0.1	Wang et al. [17]
	No.134 pegmatite dike (Jm134)	Muscovite Ar–Ar	199 ± 0.4	Wang et al. [17]
Xuebaoding ore field	Yanggonghai	Zircon U–Pb	221 ± 4	Zhang et al. [18]
	Pegmatite dike (Xm1)	Muscovite Ar–Ar	190 ± 2	Li et al. [27]
	Pegmatite dike	Muscovite Ar–Ar	195 ± 1	Zhang et al. [19]
Dahongliutan ore field	Two-mica granite	Zircon U–Pb	220 ± 2 217 ± 2	Qiao et al. [47]
	The No. 90 pegmatite dike (Dm90)	Columbite U–Pb	212 ± 2	Yan et al. [48]
		Muscovite Ar–Ar	189 ± 1	This paper
	The No. 102 pegmatite dike (Dm102)	Muscovite Ar–Ar	187 ± 1	This paper
Zhawulong ore field	Muscovite granite (ZG-1)	Zircon U–Pb	212 ± 5	This paper
	The No. 14 pegmatite dike (Zct-1)	Columbite–tantalite U–Pb	205 ± 2	This paper
	The No. 14 pegmatite dike (Zm-1)	Muscovite Ar–Ar	180 ± 1	This paper
	The No. 97 pegmatite dike (Zm-2)	Muscovite Ar–Ar	174 ± 1	This paper
Ke'eryin ore field	Two-mica granite	Zircon U–Pb	207 ± 1 205 ± 4	Zhao et al. [49]; Yue et al. [50]
	Lijiagou spodumene pegmatite dike	Zircon U–Pb	198 ± 3	Fei et al. [51]
	Muscovite pegmatite dike (Km1)	Muscovite Ar–Ar	159 ± 1	This paper

Because the closure temperature of the Ar–Ar isotope system in muscovite (300 °C–400 °C; [43–45,52,53]) is close to the lowest crystallization temperature of pegmatite (350 °C–450 °C; [54,55]), the Ar–Ar plateau ages of muscovite can represent the final crystallization age of the pegmatites. Although the closure temperature of the columbite–tantalite U–Pb system has never been reported, it should be similar to the closure temperature of the zircon U–Pb system based on the similarity between the U–Pb zircon age (216 ± 2 Ma) and the columbite–tantalite age (214 ± 2 Ma) in the Jiajika pegmatite [16]. As a result, the ages that are similar to zircon U–Pb ages can represent the initial crystallization age of pegmatite. In addition, the closure temperature of the columbite–tantalite U–Pb system can be preliminarily inferred to be approximately 700 °C–500 °C, as pegmatite crystallization began in this temperature range in the Jiajika pegmatite [56]. Therefore, it can be concluded that the crystallization of pegmatites in the Jiajika, Xuebaoding, Dahongliutan, Zhawulong, and Ke'eryin deposits finally began at approximately 223, 221, 220–217, 212, and 207–205 Ma, respectively. Furthermore, it can be supposed that crystallization of the corresponding pegmatite ceased at approximately 199–196, 195–190, 189–187, 180–174, and 159 Ma, respectively.

We then plotted the cooling paths of the main granitic pegmatite deposits in different sections of the Songpan–Ganzê orogenic belt (Figure 11). We discovered that from the outer areas (Jiajika, Xuebaoding, and Dahongliutan ore fields) to the middle area (Zhawulong ore field) and then to the inner area (Ke'eryin ore field), there was a lag from the peak in magmatic activity to the final crystallization ages of the pegmatite deposits.

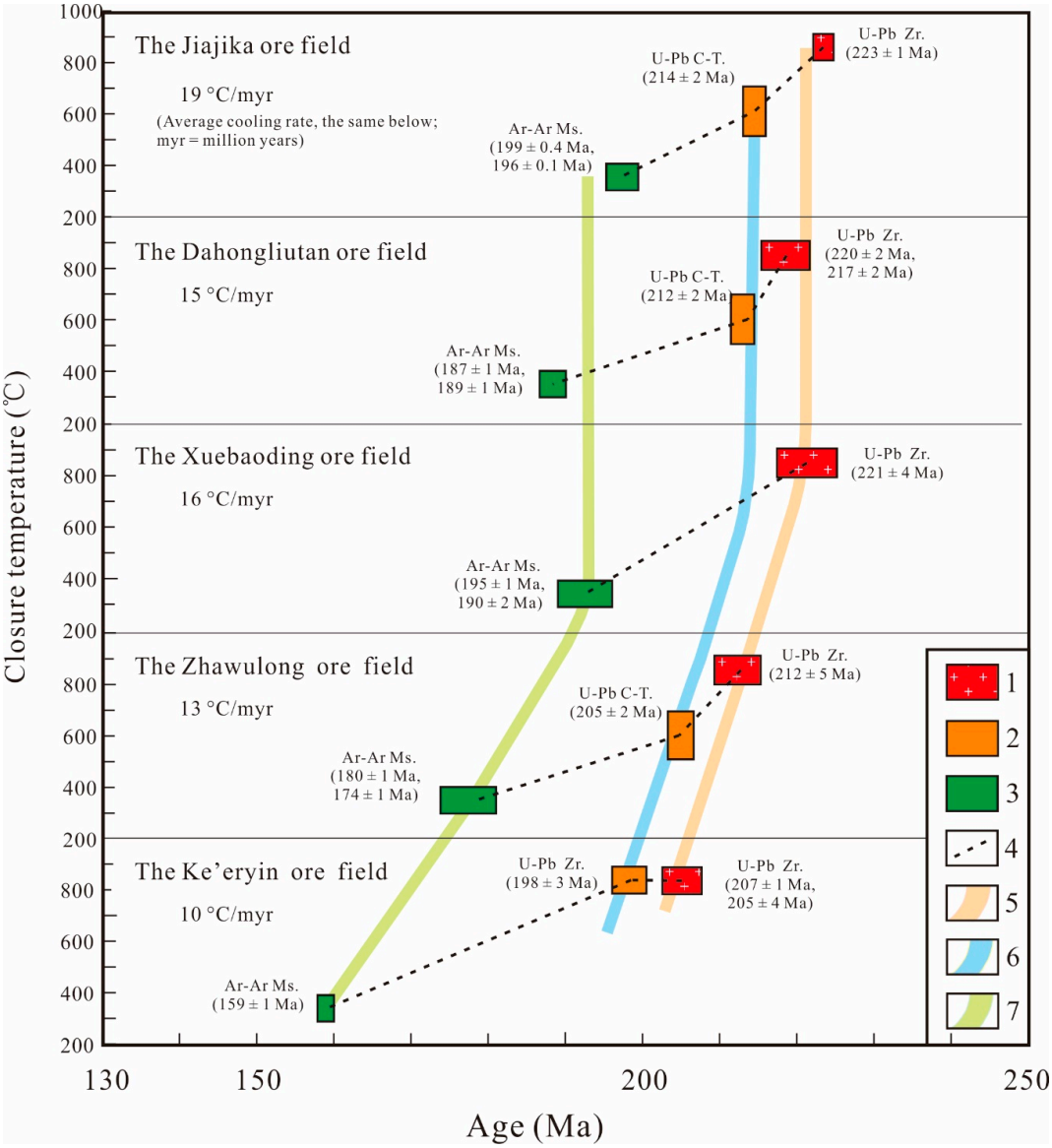

Figure 11. Cooling T–t paths in different areas of the Songpan–Ganzê orogenic belt, plotted from the closure temperatures of different isotope systems and the corresponding dating results. The widths and heights of rectangles represent the ranges in age and closure temperature, respectively. To calculate the average cooling rates, we assume that the closure temperatures of the U–Pb system in zircon and the Ar–Ar isotope system in muscovite are 850 °C and 350 °C, respectively, as described in the discussion. 1: Zircon U-Pb age of granite; 2: Zircon/columbite–tantalite U-Pb age of pegmatite; 3: Muscovite Ar–Ar age of pegmatite; 4: Inferred cooling paths; 5–7: Age comparison of rare metal deposits, 5: Granite emplacement age, 6: Initial crystallization age of pegmatite, 7: Final crystallization age of pegmatite; Ms: Muscovite; C–T: Columbite–tantalite; Zr: Zircon.

6.2. Formation Mechanism of Granite-Pegmatite Systems in the Songpan–Ganzê Orogenic Belt

It is generally believed that the LCT pegmatite and the peraluminous S-type granite system have a genetic relationship with the melting of sedimentary and/or metamorphosed sedimentary or supracrustal rocks [1,3,54,57–60]. In addition, it is generally agreed upon that the emplacement of pegmatite occurred during a period of continental collision and crustal thickening, or at the end of this period [61–63]. Crustal thickening and subsequent decompression led to melting of the mica-rich (meta)sedimentary strata, which is a potentially important source of H_2O, F, and rare metal elements. Finally, rare metal pegmatite was formed [41,64–73]. Many important rare metal deposits across

the globe, such as the Ghost Lake deposit in North America, the Greenbushes deposit in Australia, and the pegmatite province in eastern Brazil, occurred in orogenic belts and formed through multistage magmatic superimposition in an orogenic tectonic setting [12,41,74–76].

The Songpan–Ganzê orogenic belt formed during the convergence of the Yangtze, Qiangchang–Changdu, and North China blocks in the Indosinian period, accompanied by the closure of the Paleo-Tethys oceanic basin [15,77–80]. During the collisions, the northward and southward tectonic stresses caused decollement to occur between the basement and the cap rock (Triassic sediments) [13,15,81], accompanied by extensive folding and thrusting that led to large-scale crustal shortening and thickening. During deformation, the temperature increase may have been promoted by shear heating along the decollement [82,83]. Finally, the accumulated heating led to the melting of Triassic metaturbidites and the widely distributed rare metal deposit formations [16–19,27,47–51] from the outer areas (Jiajika, Xuebaoding, and Dahongliutan ore fields) to the middle area (the Zhawulong ore field) and then to the central area (Ke'eryin ore field), as illustrated in Figure 11 and Table 1.

6.3. Implications of Pegmatite Deposits for Orogeny in the Songpan–Ganzê Orogenic Belt

The granite-pegmatite systems in the Songpan–Ganzê orogenic belt resulted from tectonic–thermal movements caused by collisions of the Yangtze, Qingtang-Changdu, and North China blocks. As illustrated in Figure 11, from the outer to the middle to the inner areas of the Songpan–Ganzê orogeny belts, the granite emplacement ages as well as the initial and final crystallization ages of pegmatites become younger synchronously, indicating the tectonic–thermal stress transfer process. Furthermore, the lag from the peak in magmatic activities to the final crystallization of large spodumene pegmatite dikes increased in the same order. The lags observed in the Jiajika, Xuebaoding, and Dahongliutan ore fields in the outer areas of the orogeny belt were approximately 26–28, 21–29, and 27–36 million years, respectively, and the lags observed in the Zhawulong and Ke'eryin ore fields located in the middle and central areas of the orogeny belt were approximately 32–44 and 43–49 million years, respectively. The features discussed above indicate that the magma cooling rates of the Jiajika, Dahongliutan, and Xuebaoding deposits in the outer area of the orogenic belt are highest, while those of the Ke'eryin deposit in the central area are lowest, as shown in Figure 11.

These cooling rates are in good agreement with the stages and scales of granitic magma emplacements in these pegmatite deposits. Single-stage magma emplacement with a relatively small outcrop area occurred in the Jiajika, Dahongliutan, and Xuebaoding deposits, while multi-stage magma emplacement with a large outcrop area occurred in the Ke'eryin ore field. The residual Triassic laccolith at the top of the complex granitic intrusions in these ore fields indicates that these granitic intrusions underwent similar degrees of uplift erosions (Figures 2–5), eliminating the effect of erosion on the emergence of these magma intrusive stages and scales. The large-scale outcropping and multistage of granite with a low cooling rate may be due to the fact that Ke'eryin is located in the center of the Songpan–Ganzê orogenic belt, in which there was a convergence of northward and southward thermal stresses resulting from collisions between the Yangtze and Qiangtang–Chagndu blocks, and the Yangtze and North China blocks, respectively [81]. As a result, the convergence of thermal stress in two directions led to greater heat flow and a slower cooling rate, resulting in extensive continuous magmatic activity and a high melting point. Adequate heat and a slow cooling rate will lead to crystallization and differentiation of magma over a long period of time, forming greater rare metal deposits with potential Li_2O reserves of 7,000,000 tons, including the Lijiagou, Dangba, and Yelonggou deposits in the Ke'eryin ore field [25].

The above-mentioned temporal and spatial regularities indicate that the tectonic–thermal stress transfer process occurred in the northward and southward directions from the outer areas to the inner areas of the Songpan–Ganzê orogenic belt. On the basis of the dating results in this study, we propose a model for the orogenic processes of the Songpan–Ganzê orogenic belt (Figure 12). When bidirectional contracting stress was transferred from the collision boundaries in the Yangtze, Qiangtang–Changdu, and North China blocks, magmatism occurred in the Jiajika, Xuebaoding, and Dahongliutan ore fields

approximately 223–217 Ma. The cooling rates in these regions were relatively high, resulting in the rare metal element pegmatite being formed in the relatively short range of 199–187 Ma. When the tectonic stress was transferred into the Zhawulong ore field, massive magma intruded approximately 212 Ma, and the formation of spodumene pegmatite dikes occurred during a relatively late stage lasting until approximately 180–174 Ma. Finally, the northward and southward tectonic stress converged in the Ke'eryin area, leading to magmatic activity approximately 207–205 Ma with a subsequent long pegmatite crystallization period that lasted until approximately 159 Ma.

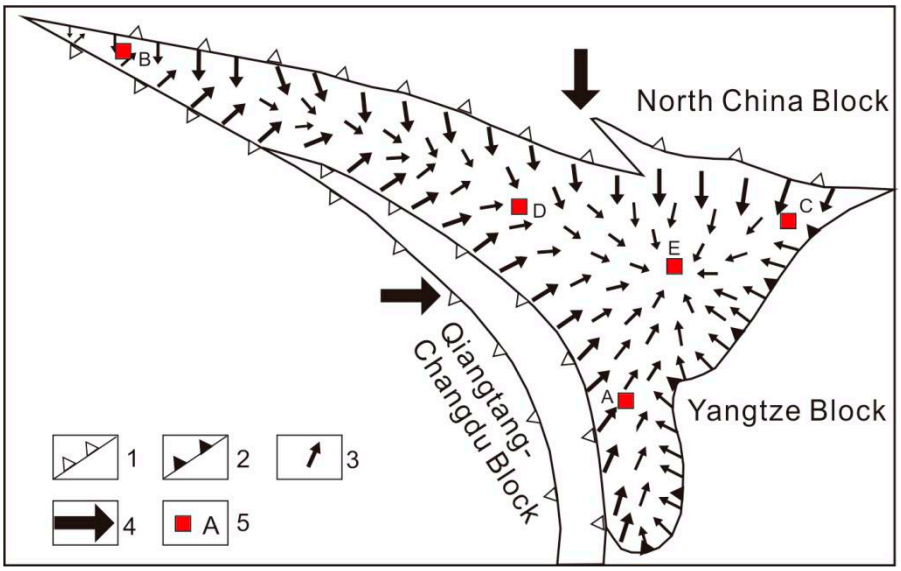

Figure 12. Orogenic process inferred from the ore-forming ages of pegmatite deposits in the Songpan–Ganzê orogenic belt. 1: Abduction zone; 2: Displacement fault; 3: Tectonic stress; 4: Direction of collision and pressure; 5: Pegmatite deposits; A: Jiajika deposit; B: Dahongliutan deposit; C: Xuebaoding deposit; D: Zhawulong deposit; E: Ke'eryin deposit.

7. Conclusions

In the Songpan–Ganzê orogenic belt in China, the Jiajika, Dahongliutan, Xuebaoding, Zhawulong, and Ke'eryin granitic pegmatite deposits, which have different ore-formation ages, are located in the southern, northern, western, and central areas, and the center of the eastern area in the Songpan–Ganzê orogenic belt, respectively. The No. 90 and No. 102 spodumene pegmatite dikes in the Dahongliutan deposit indicated muscovite Ar–Ar plateau ages of 187.0 ± 1.1 Ma and 189.4 ± 1.1 Ma, respectively. In the Zhawulong ore field, the No. 14 and No. 97 spodumene pegmatite dikes indicated muscovite Ar–Ar plateau ages of 179.6 ± 1.0 Ma and 174.3 ± 0.9 Ma, respectively. Columbite–tantalites from the No. 14 spodumene pegmatite dikes yielded a U–Pb age of 204.5 ± 1.8 Ma, and zircons from the Zhawulong granite yielded a U–Pb age of 211.6 ± 5.2 Ma. In the Ke'eryin ore field, the spodumene pegmatite was dated and displayed muscovite Ar–Ar plateau ages of 159.0 ± 1.4 Ma. Combining previous age dating data, we concluded that the granitic magma in the Jiajika, Xuebaoding, Dahongliutan, Zhawulong, and Ke'eryin deposits intruded into Triassic metaturbidites at approximately 223, 221, 220–217, 212, and 207–205 Ma, respectively, and that the crystallization of the corresponding pegmatite ceased at approximately 199–196, 195–190, 189–187, 180–174, and 159 Ma, respectively.

Combining the previous dating results for pegmatite and pegmatite-related granite and regional granitic intrusions with different isotopic dating systems, we were able to derive the cooling paths in the different pegmatite deposits. We discovered that from the outer areas of the orogenic belt to the inner areas, the peak in magmatic activity and the final crystallization ages of the pegmatite deposits tended to lag, implying the migration process of tectonic stress. More heat flow is gathered in the inner area at the convergent center of thermal stress in two directions, which leads to extensive continuous

magmatic activity and a slow cooling rate. Adequate heat and a slow cooling rate lead to secondary crystallization and differentiation of magma, further forming greater rare metal deposits.

On the basis of the above regularity, we conclude that during the late Indosinian period, the bidirectional tectonic stresses in the Songpan–Ganzê orogenic belt resulting from the collision between the North China block, Qiangtang–Changdu block, and Yangtze block, were transferred from the outer area to the inner area of the orogenic belt. These processes may have resulted in magmatic activity and the mineralization of pegmatite dikes in the Jiajika, Xuebaoding, Dahongliutan, Zhawulong, and Ke'eryin ore fields during orogeny.

Author Contributions: P.L., J.L. and X.X. performed the analysis of the results and the interpretation of the data; J.L. wrote the initial draft of the paper which was further modified by P.L. after further discussions with all the authors; I.-M.C. and D.W. revised the paper and refined the language.

Funding: This study was funded by the National Natural Science Foundation of China (41372088), the National Key R and D Program of China (2017YFC0602701), the Chinese National Non–Profit Institute Research Grant of CAGS-IMR (K1409), and the Research Program of Department of Nature Resources of Hunan Province (grant number 2018–02).

Acknowledgments: We thank Chao Li, Linghao Zhao and Qinggao Yan for their help during zircon U–Pb dating analyses. Special thanks to Xudong Che for his guidance for columbite–tantalite U–Pb dating.

Conflicts of Interest: The authors declare no conflict of interest.

Appendix A

Table A1. $^{40}Ar/^{39}Ar$ step-heating data for muscovite samples extracted from the spodumene pegmatites of the Dahongliutan, Zhawulong, and Ke'eryin ore fields.

T(°C)	$(40Ar/39Ar)_m$	$(36Ar/39Ar)_m$	$(37Ar_0/39Ar)_m$	F	39Ar (Cum.) (%)	Age (Ma)	±1σ (Ma)
Dm90 muscovite W = 27.27 mg J = 0.004527							
700	111.9480	0.2994	0.0000	23.4583	0.15	182.0	12.0
760	46.2993	0.0820	0.3557	22.1028	0.66	172.0	4.2
800	45.9735	0.0751	0.0463	23.7776	2.49	184.4	2.0
840	35.6290	0.0391	0.0758	24.0721	5.52	186.6	1.9
880	28.4870	0.0137	0.0107	24.4274	15.82	189.2	1.8
920	24.7410	0.0020	0.0053	24.1543	46.29	187.2	1.8
950	24.6020	0.0014	0.0096	24.1757	62.75	187.4	1.8
980	24.8512	0.0017	0.0037	24.33	70.5	188.5	1.8
1020	25.0782	0.0039	0.0725	23.9286	75.22	185.5	1.8
1060	25.0704	0.0037	0.0402	23.9818	79.92	185.9	1.8
1130	24.9181	0.0024	0.0161	24.2072	90.08	187.6	1.8
1200	24.3992	0.0039	0.0000	23.235	98.7	186.8	1.8
1400	26.7676	0.0089	0.0413	24.1321	100	187.0	2.3
Plateau Age = 187.0 ± 1.1 Ma							
Dm102 muscovite W = 27.05 mg J = 0.004533							
700	114.2605	0.3392	1.3696	14.128	0.23	112.0	12.0
760	48.2186	0.0796	0.0000	24.6884	1.5	191.4	2.3
800	41.0508	0.0575	0.0183	24.068	2.95	186.8	2.2
840	35.1192	0.0365	0.0579	24.3244	5.93	188.7	1.9
880	29.2235	0.0151	0.0077	24.7625	13.62	191.9	1.8
920	25.2772	0.0030	0.0071	24.3867	46.81	189.2	1.8
950	24.9819	0.0016	0.0008	24.5038	61.11	190.0	1.8
980	25.3326	0.0021	0.0000	24.6955	67.12	191.4	1.8
1020	25.5773	0.0040	0.0148	24.3907	71.14	189.2	1.8
1060	25.5313	0.0048	0.0377	24.0993	75.27	187.0	1.8
1200	24.8587	0.0023	0.0076	24.1793	97.22	187.6	1.8
1400	25.6757	0.0041	0.0106	24.471	100	189.8	1.9
Plateau Age = 189.4 ± 1.1 Ma							

Table A1. *Cont.*

T(°C)	$(40Ar/39Ar)_m$	$(36Ar/39Ar)_m$	$(37Ar_0/39Ar)_m$	F	39Ar (Cum.) (%)	Age (Ma)	±1σ (Ma)
ZM-1 muscovite W = 15.42 mg J = 0.004750							
700	270.8757	0.8839	0.0638	9.6789	0.30	81.1	14.7
770	101.9434	0.2777	0.0000	19.8916	2.22	162.9	4.2
830	60.9972	0.1296	0.0000	22.6841	6.24	184.6	2.0
880	31.1068	0.0293	0.0040	22.4389	17.07	182.7	0.5
920	23.4427	0.0047	0.0000	22.0476	50.97	179.7	0.3
950	23.4546	0.0050	0.0075	21.9673	58.43	179.1	0.4
990	24.2049	0.0069	0.0000	22.1640	74.37	180.6	0.3
1030	26.1738	0.0141	0.0000	21.9897	82.39	179.2	0.5
1080	26.9635	0.0173	0.0098	21.8437	90.26	178.1	0.4
1160	23.5498	0.0056	0.0000	21.8758	98.42	178.4	0.4
1260	28.1971	0.0211	0.0000	21.9528	99.76	179.0	1.0
1400	46.6306	0.0786	0.0000	23.4097	100.00	190.2	9.2
Plateau Age = 179.6 ± 1.0 Ma							
ZM-2 muscovite W = 16.93 mg J = 0.004779							
700	346.3185	1.1314	0.0950	12.00076	0.35	100.6	17.9
760	155.2648	0.4345	0.0112	26.85222	2.00	217.8	6.3
800	100.0595	0.2638	0.0155	22.11302	4.12	181.2	3.9
850	48.3097	0.0902	0.0155	21.66208	7.48	177.7	1.4
890	27.3878	0.0199	0.0073	21.50775	15.81	176.5	0.4
930	22.6281	0.0050	0.0017	21.15015	36.06	173.7	0.3
970	22.4772	0.0042	0.0000	21.22109	56.45	174.3	0.3
1010	23.2571	0.0071	0.0000	21.15922	67.81	173.8	0.3
1060	25.5231	0.0149	0.0096	21.11696	76.19	173.5	0.4
1120	25.3077	0.0134	0.0011	21.32966	86.20	175.1	0.4
1200	22.8419	0.0056	0.0033	21.18531	98.81	174.0	0.3
1240	25.9042	0.0159	0.0000	21.19262	99.63	174.0	1.3
1280	36.2060	0.0505	0.0000	21.26801	99.86	174.6	3.6
1400	66.4398	0.1495	0.0000	22.24769	100.00	182.3	7.8
Plateau Age = 174.3 ± 0.9 Ma							
Km1 muscovite W = 46.00 mg J = 0.011771							
500	35.5959	0.0953	0.1089	7.4408	0.24	151	12
600	18.4300	0.0362	0.1884	7.7409	0.37	157.3	6.6
700	26.6486	0.0695	0.0635	6.1205	0.73	126	11
800	19.9345	0.0458	0.0276	6.4044	1.26	131.1	5.8
900	11.1333	0.0120	0.0164	7.5871	3.17	154.3	1.5
1000	9.7808	0.0065	0.0104	7.8681	11.46	159.8	1.6
1050	8.3920	0.0021	0.0016	7.7543	35.48	157.6	1.6
1100	8.0570	0.0012	0.0017	7.698	54.53	156.5	1.6
1200	8.2419	0.0019	0.0022	7.6761	65.35	156.1	1.5
1300	8.0557	0.0011	0.0012	7.718	88.86	156.9	1.6
1400	8.0256	0.0007	0.0018	7.8019	100	158.5	1.5
Plateau Age = 159.0 ± 1.4 Ma							

F = 40Ar*/39Ar, is the ratio of radiogenic Argon40 and Argon39.

Table A2. LA-ICP-MS U–Pb data for zircons and columbite–tantalites from the Zhawulong deposit.

Grain Spot	Th	U	Th/U	Isotopic Ratios						Age(Ma)					
				207Pb/206Pb	1σ	207Pb/235U	1σ	206Pb/238U	1σ	207Pb/206Pb	1σ	207Pb/235U	1σ	206Pb/238U	1σ
ZG-1-1	222.2	2227.0	0.10	0.0519	0.0013	0.2517	0.0071	0.0335	0.0016	282.1	55.4	227.9	5.7	212.4	9.7
ZG-1-2	62.0	1114.6	0.06	0.0499	0.0011	0.2335	0.0057	0.0337	0.0016	189.8	49.2	213.1	4.7	213.6	9.7
ZG-1-3	200.8	367.0	0.55	0.0603	0.0016	0.7674	0.0281	0.0939	0.0044	613.8	56.8	578.3	16.2	578.8	25.8
ZG-1-4	77.7	675.4	0.12	0.0521	0.0015	0.2340	0.0075	0.0333	0.0016	291.1	64.5	213.5	6.2	211.1	9.7
ZG-1-5	83.5	695.9	0.12	0.0500	0.0014	0.2371	0.0074	0.0336	0.0016	194.5	63.1	216.1	6.0	212.8	9.8
ZG-1-6	58.3	551.4	0.11	0.0540	0.0032	0.2382	0.0159	0.0321	0.0016	370.5	129.6	216.9	13.1	203.9	9.9
ZG-1-7	165.0	398.6	0.41	0.0541	0.0018	0.4951	0.0211	0.0643	0.0030	376.9	74.7	408.3	14.4	402.0	18.4
ZG-1-8	88.7	2027.5	0.04	0.0528	0.0011	0.2360	0.0055	0.0328	0.0015	321.9	46.1	215.1	4.5	207.9	9.5
ZG-1-9	282.6	1527.5	0.19	0.0501	0.0011	0.2369	0.0058	0.0338	0.0016	198.8	49.1	215.8	4.7	214.1	9.8
ZG-1-10	1026.9	1457.4	0.70	0.0511	0.0019	0.2321	0.0097	0.0323	0.0015	245.7	83.3	211.9	8.0	205.2	9.6
ZG-1-11	2448.1	770.5	3.18	0.0516	0.0017	0.2364	0.0088	0.0333	0.0016	266.3	74.7	215.4	7.2	211.2	9.8
ZG-1-12	201.1	427.5	0.47	0.0710	0.0011	1.4007	0.0329	0.1473	0.0068	956.6	32.3	889.2	13.9	885.6	38.4
ZG-1-13	912.5	12605.2	0.07	0.4446	0.0050	1.4477	0.0193	0.0300	0.0014	4067.3	16.6	908.9	8.0	190.5	8.7
ZG-1-14	156.6	165.8	0.94	0.0591	0.0023	0.5613	0.0271	0.0737	0.0035	570.9	81.1	452.4	17.6	458.6	21.1
ZG-1-15	53.3	644.8	0.08	0.0521	0.0016	0.2370	0.0081	0.0341	0.0016	290.7	68.5	215.9	6.7	215.9	10.0
ZG-1-16	70.7	258.8	0.27	0.0622	0.0019	0.7667	0.0326	0.0913	0.0043	682.5	65.3	577.8	18.8	563.0	25.5
ZG-1-17	55.0	623.6	0.09	0.0529	0.0025	0.2412	0.0125	0.0340	0.0016	325.0	102.1	219.4	10.2	215.5	10.2
ZG-1-18	116.7	250.8	0.47	0.1845	0.0025	10.1794	0.3342	0.3985	0.0186	2694.0	22.5	2451.2	30.4	2162.1	85.7
ZG-1-19	677.1	655.7	1.03	0.0650	0.0014	0.9601	0.0299	0.1075	0.0050	773.0	45.4	683.4	15.5	658.0	29.3
ZG-1-20	321.4	174.0	1.85	0.0595	0.0020	0.7615	0.0351	0.0925	0.0044	584.7	72.3	574.9	20.2	570.1	25.9
ZG-1-21	405.4	837.8	0.48	0.0543	0.0010	0.4983	0.0118	0.0650	0.0030	381.9	42.7	410.6	8.0	405.8	18.4
ZG-1-22	17.4	1873.8	0.01	0.0519	0.0023	0.2419	0.0122	0.0331	0.0016	280.1	99.2	220.0	10.0	209.6	10.0
ZG-1-23	32.1	792.4	0.04	0.0520	0.0018	0.2410	0.0096	0.0332	0.0016	286.1	78.8	219.2	7.8	210.3	9.8
ZG-1-24	92.7	1029.7	0.09	0.1130	0.0040	0.4594	0.0194	0.0277	0.0014	1847.9	62.9	383.8	13.5	176.4	8.5
ZG-1-25	520.7	339.9	1.53	0.1019	0.0034	0.5545	0.0227	0.0392	0.0019	1658.6	60.2	447.9	14.8	248.1	11.7
ZG-1-26	248.6	2164.3	0.11	0.0502	0.0011	0.2346	0.0056	0.0344	0.0016	204.3	48.4	214.0	4.6	217.7	10.1
ZG-1-27	504.3	1015.3	0.50	0.0739	0.0015	0.7688	0.0207	0.0713	0.0034	1039.7	40.3	579.0	11.9	444.2	20.2
ZG-1-28	8.1	854.3	0.01	0.0618	0.0021	0.2416	0.0090	0.0332	0.0016	668.0	70.2	219.8	7.4	210.3	9.9
Zct-1-1	0.4	56.3	0.01	0.0705	0.0010	0.3386	0.0066	0.0349	0.0006	941.9	29.7	296.1	5.0	221.0	3.6
Zct-1-2	0.4	60.5	0.01	0.0665	0.0010	0.3214	0.0062	0.0351	0.0006	822.9	30.2	282.9	4.8	222.1	3.7
Zct-1-3	1.9	196.5	0.01	0.0556	0.0007	0.2431	0.0043	0.0317	0.0005	435.6	26.2	221.0	3.5	201.5	3.3
Zct-1-4	845.4	733.0	1.15	0.4460	0.0044	116.9998	1.9078	1.9041	0.0314	4071.9	14.7	4844.1	16.4	6872.7	69.8
Zct-1-5	2.2	149.0	0.01	0.0974	0.0011	0.5194	0.0089	0.0387	0.0006	1574.1	21.0	424.7	5.9	244.9	4.0
Zct-1-6	0.6	71.7	0.01	0.0847	0.0011	0.3986	0.0073	0.0342	0.0006	1308.7	25.6	340.6	5.3	216.5	3.6
Zct-1-7	1.3	126.1	0.01	0.0559	0.0007	0.2452	0.0045	0.0318	0.0005	449.5	28.3	222.6	3.7	201.9	3.3
Zct-1-8	1.1	106.4	0.01	0.0644	0.0008	0.3138	0.0057	0.0354	0.0006	755.6	26.8	277.1	4.4	224.0	3.7
Zct-1-9	0.8	86.8	0.01	0.0569	0.0008	0.2502	0.0048	0.0319	0.0005	488.5	31.3	226.7	3.9	202.4	3.3
Zct-1-10	1.0	114.8	0.01	0.0536	0.0007	0.2372	0.0044	0.0321	0.0005	354.0	30.0	216.1	3.6	203.8	3.3
Zct-1-11	0.3	51.4	0.01	0.0726	0.0011	0.3388	0.0066	0.0339	0.0006	1003.9	29.9	296.3	5.0	214.6	3.5
Zct-1-12	0.2	30.9	0.01	0.0652	0.0011	0.3219	0.0069	0.0358	0.0006	781.6	36.1	283.3	5.3	226.9	3.8
Zct-1-13	4.5	295.4	0.02	0.0562	0.0006	0.2484	0.0043	0.0321	0.0005	460.5	25.3	225.3	3.5	203.5	3.3
Zct-1-14	1.3	110.5	0.01	0.0553	0.0008	0.2430	0.0046	0.0319	0.0005	425.9	30.6	220.9	3.8	202.2	3.3
Zct-1-15	0.6	71.8	0.01	0.0667	0.0009	0.3306	0.0062	0.0360	0.0006	826.7	28.6	290.0	4.7	228.0	3.7
Zct-1-16	2.0	129.8	0.02	0.1922	0.0021	1.0484	0.0176	0.0396	0.0007	2760.8	17.5	728.1	8.7	250.4	4.1
Zct-1-17	0.7	130.6	0.01	0.0593	0.0008	0.2719	0.0049	0.0333	0.0006	576.4	27.2	244.2	3.9	211.2	3.5
Zct-1-18	0.6	69.0	0.01	0.0720	0.0010	0.3706	0.0069	0.0374	0.0006	985.3	27.5	320.1	5.1	236.5	3.9
Zct-1-19	0.9	101.9	0.01	0.0543	0.0008	0.2350	0.0045	0.0314	0.0005	382.7	32.0	214.3	3.7	199.4	3.3
Zct-1-20	0.7	125.7	0.01	0.0618	0.0008	0.2876	0.0052	0.0338	0.0006	668.0	26.7	256.6	4.1	214.0	3.5
Zct-1-21	1.2	103.7	0.01	0.0577	0.0008	0.2823	0.0051	0.0355	0.0006	519.5	28.4	252.5	4.1	224.8	3.7
Zct-1-22	0.8	87.7	0.01	0.0552	0.0008	0.2544	0.0048	0.0335	0.0006	418.6	30.6	230.1	3.9	212.2	3.5
Zct-1-23	1.1	119.8	0.01	0.0536	0.0007	0.2438	0.0045	0.0330	0.0006	353.6	29.2	221.5	3.6	209.4	3.4
Zct-1-24	0.0	100.2	0.00	0.0687	0.0009	0.3198	0.0058	0.0338	0.0006	890.0	26.5	281.8	4.5	214.2	3.5
Zct-1-25	1.6	160.9	0.01	0.0525	0.0007	0.2328	0.0042	0.0322	0.0005	307.8	28.1	212.5	3.4	204.2	3.3
Zct-1-26	1.9	179.5	0.01	0.0528	0.0006	0.2356	0.0042	0.0324	0.0005	319.7	27.3	214.8	3.4	205.5	3.4
Zct-1-27	0.5	72.8	0.01	0.0653	0.0009	0.3254	0.0061	0.0362	0.0006	783.4	28.6	286.1	4.7	229.1	3.8
Zct-1-28	0.0	105.7	0.00	0.0692	0.0009	0.3187	0.0058	0.0335	0.0006	903.3	26.3	280.9	4.5	212.1	3.5
Zct-1-29	0.5	69.5	0.01	0.0621	0.0009	0.2753	0.0053	0.0322	0.0005	675.7	31.1	246.9	4.3	204.3	3.4
Zct-1-30	0.9	97.1	0.01	0.0551	0.0008	0.2432	0.0046	0.0321	0.0005	414.0	30.1	221.0	3.7	203.4	3.3
Zct-1-31	0.9	125.8	0.01	0.0560	0.0007	0.2445	0.0045	0.0317	0.0005	450.0	28.4	222.1	3.7	201.3	3.3
Zct-1-32	0.9	89.0	0.01	0.0589	0.0009	0.2501	0.0050	0.0308	0.0005	561.9	33.0	226.7	4.1	195.8	3.2
Zct-1-33	0.8	75.4	0.01	0.0631	0.0009	0.2780	0.0054	0.0320	0.0005	710.7	30.8	249.1	4.3	203.0	3.3
Zct-1-34	0.7	63.4	0.01	0.0594	0.0009	0.2727	0.0055	0.0333	0.0006	580.6	33.5	244.8	4.4	211.4	3.5
Zct-1-35	1.2	125.8	0.01	0.0536	0.0007	0.2412	0.0044	0.0327	0.0005	352.6	29.1	219.4	3.6	207.3	3.4
Zct-1-36	1.9	182.9	0.01	0.0638	0.0008	0.3119	0.0055	0.0355	0.0006	734.1	24.9	275.7	4.2	224.9	3.7
Zct-1-37	0.7	85.8	0.01	0.0555	0.0008	0.2479	0.0048	0.0324	0.0005	431.9	31.4	224.9	3.9	205.7	3.4
Zct-1-38	0.9	88.8	0.01	0.0538	0.0008	0.2403	0.0046	0.0324	0.0005	364.3	31.6	218.6	3.7	205.5	3.4
Zct-1-39	0.5	63.1	0.01	0.0632	0.0009	0.2956	0.0058	0.0340	0.0006	714.9	31.4	263.0	4.5	215.2	3.5
Zct-1-40	0.9	100.2	0.01	0.0555	0.0008	0.2750	0.0051	0.0360	0.0006	431.1	29.3	246.7	4.1	227.9	3.7

References

1. Černý, P. Rare-element granite pegmatites: Part II. Regional to global environments and petrogenesis. *Geosci. Can.* **1991**, *18*, 68–81.
2. Linnen, R.L.; Lichtervelde, M.V.; Černý, P. Granitic pegmatites as sources of strategic metals. *Elements* **2012**, *8*, 275–280. [CrossRef]
3. Ginsburg, A.I.; Timofeev, I.N.; Feldman, L.G. *Osnovy Geologii Granitnykh Pegmatitov (Principles of Geology of Granitic Pegmatites)*; Nedra: Moscow, Russia, 1979. (In Russian)
4. McCauley, A.; Bradley, D.C. Global age distribution of granitic pegmatites. *Can. Mineral.* **2014**, *52*, 18–190. [CrossRef]
5. Tkachev, A.V.; Rundqvist, D.V.; Vishnevskaya, N.A. Comparison of Supercontinent Cycles in the Metallogeny of Rare Earth Elements. *Dokl. Earth Sci.* **2018**, *480*, 730–734. [CrossRef]
6. Tkachev, A.V. *Evolution of Metallogeny of Granitic Pegmatites Associated with Orogens Throughout Geological Time*; Geological Society Special Publication: London, UK, 2011; Volume 350, pp. 7–24.
7. Pedrosa, A.C.; Lobato, L.M.; Noce, C.M. Cambrian pegmatitic and hydrothermal mineral deposits: The last mineralization record prior to the south Atlantic opening in eastern Brazil. In Proceedings of the 31st Internal Geological Congress, Rio de Janeiro, Brazil, 6–17 August 2000; Volume 1.
8. Galetskiy, L.S. Perga beryllium deposit of the Ukranian shield as the geological phenomena. In Proceedings of the 31st Internal Geological Congress, Rio de Janeiro, Brazil, 6–17 August 2000; Volume 1.
9. Mints, M.V. Paleoproterozoic tectonic evolution and related metallogeny of the Eastern Baltic shield and Voronezh crystalline massif of the east European craton. In Proceedings of the 31st Internal Geological Congress, Rio de Janeiro, Brazil, 6–17 August 2000; Volume 1.
10. Mohammedyasin, M.S.; Desta, Z.; Getaneh, W. Petrography and geochemistry of the primary ore zone of the Kenticha rare metal granite-pegmatite field, Adola Belt, Southern Ethiopia: Implications for ore genesis and tectonic setting. *J. Afr. Earth Sci.* **2017**, *134*, 73–84. [CrossRef]
11. Makrygina, V.A.; Suvorova, L.F.; Antipin, V.S.; Makagon, V.M. Rare-metal pegmatoid granites, markers of the beginning of the Hercynian within-plate stage in the Ol'khon region of the Baikal area. *Russ. Geol. Geophys.* **2018**, *59*, 1626–1639. [CrossRef]
12. Li, J.; Zou, T.; Liu, X.; Wang, D.; Ding, X. The Metallogenetic Regularities of Lithium Deposits in China. *Acta Geol. Sin.* **2015**, *89*, 652–670, (In Chinese with English abstract).
13. Roger, F.; Malavieille, J.; Leloup, P.H.; Calassou, S.; Xu, Z. Timing of granite emplacement and cooling in the Songpan-Garze fold belt (eastern Tibetan Plateau) with tectonic implications. *J. Asian Earth Sci.* **2004**, *22*, 465–481. [CrossRef]
14. Harrowfield, M.J.; Wilson, C.J. Indosinian deformation of the Songpan Garze Fold Belt, northeast Tibetan Plateau. *J. Struct. Geol.* **2005**, *27*, 101–117. [CrossRef]
15. Xu, Z.; Wang, R.; Zhao, Z.; Fu, X. On the structural back grounds of the large-scale "hard-rock type"lithium ore belts in China. *Acta Geol. Sin.* **2018**, *92*, 1091–1106, (In Chinese with English abstract).
16. Hao, X.; Fu, X.; Liang, B.; Yuan, Y.; Pan, M.; Tang, Y. Formation ages of granite and X03 pegmatite vein in Jiajika, western Sichuan, and their geological significance. *Miner. Depos.* **2015**, *34*, 1199–1208, (In Chinese with English abstract).
17. Wang, D.; Li, J.; Fu, X. $^{40}Ar/^{39}Ar$ dating for the Jiajika pegmatite-type rare metal deposit in western Sichuan and its significance. *Geochimica* **2005**, *34*, 541–547, (In Chinese with English abstract).
18. Zhang, H.; Zhang, L.; Harris, N.; Jin, L.; Yuan, H. U–Pb zircon ages, geochemical and isotopic compositions of granitoids in Songpan–Garze fold belt, eastern Tibetan Plateau: Constraints on petrogenesis and tectonic evolution of the basement. *Contrib. Miner. Petrol.* **2006**, *152*, 75–88. [CrossRef]
19. Zhang, D.; Peng, J.; Coulson, I.; H, L.; Li, S. Cassiterite U–Pb and muscovite ^{40}Ar–^{39}Ar age constraints on the timing of mineralization in the Xuebaoding Sn–W–Be deposit, western China. *Ore Geol. Rev.* **2014**, *62*, 315–322. [CrossRef]
20. Chen, S.F.; Wilson, C.J. Emplacement of the Longmen Shan Thrust-Nappe Belt along the eastern margin of the Tibetan Plateau. *J. Struct. Geol.* **1996**, *18*, 413–440. [CrossRef]
21. Liu, Z.; Pei, X.; Li, R.; Li, Z.; Zhang, X.; Liu, Z.; Chen, G.; Chen, Y.; Ding, S.; Guo, J. LA-ICP-MS zircon U–Pb geochronology of the two suites of ophiolites atthe Buqingshan area of the Acnyemaqen Orogenic Belt in the Southern Marginof East Kunlun and its tectonic implication. *Acta Geol. Sin.* **2011**, *85*, 185–195, (In Chinese with English abstract).

22. Qiu, D.Z.; Xie, Y.; Zhao, Z.; Rong, L.; Yang, P.; Zhang, D. An analysis of the oil and gas system in the reformed basin: a case study of the basin-mountain transitional area on the western side of the Xuefeng Mountain. *Geol. Bull. China* **2012**, *31*, 1781–1794, (In Chinese with English abstract).
23. Zou, T.; Li, Q. *Rare and Rare Earth Metallic Deposit in Xinjiang, China*; Geological Publishing House: Beijing, China, 2005; pp. 1–284. (In Chinese)
24. Li, J.; Fu, X.; Zou, T.; Wang, D. Prospecting breakthrough of and outside prospecting prospect analysis of Jiajika lithium deposit. *Miner. Depos.* **2014**, *33*, 1175–1176, (In Chinese with English abstract).
25. Wang, D.; Liu, L.; Dai, H.; Liu, S.; Hou, J.; Wu, X. Discussion on particularity and prospecting direction of large and Super-large spodumene deposits. *Earth Sci.* **2017**, *42*, 2243–2257, (In Chinese with English abstract).
26. Wang, H.; Li, P.; Ma, H.; Zhu, B.; Qiu, L.; Zhang, X.; Dong, R.; Zhou, K.; Wang, M.; Wang, Q.; et al. Discovery of the Bailongshan superlarge lithium-rubidium deposit in Karakorum, Hetian, Xinjiang, and its prospecting implication. *Geotecton. Metallog.* **2017**, *41*, 1053–1062, (In Chinese with English abstract).
27. Li, J.; Wang, D.; Zhang, D.; Fu, X. *Mineralizing Mechanism and Continental Geodynamics of Typical Pegmatite Deposits in Western Sichuan, China*; Atomic Energy Press: Beijing, China, 2007; p. 187, (In Chinese with English abstract).
28. Li, X.; Li, J.; Liu, Y.; Xiong, C. Geochemical features of muscovite granite in the Zhawulong granitic pegmatite type rare metal deposit, western Sichuan. *Geol. Rev.* **2018**, *64*, 231–242.
29. Cao, Z.; Zheng, J.; Li, Y.; Ren, J.; Xu, S.; Wang, R. The Ore fluid and its tracing and dating in the Xuebaoding beryl-scheelite vein deposit, China. *Sci. China* **2002**, *45*, 719–729.
30. Li, J.; Wang, D.; Fu, X. $^{40}Ar/^{39}Ar$ Ages of the Ke'eryin pegmatite type rare metal deposit, western Sichuan, and its tectonic Significances. *Acta Geol. Sin.* **2006**, *80*, 843–848, (In Chinese with English abstract).
31. Wang, S.; Sang, H.; Hu, S.; Qiu, J. ^{40}Ar–^{39}Ar age determination using 49-2 reactor and ^{40}Ar–^{39}Ar age spectrum for amphibolite for Qiannan, China. *Acta Petrol. Sin.* **1985**, *2*, 35–44, (In Chinese with English abstract).
32. Chen, W.; Zhang, Y.; Ji, Q. The magmatism and deformation times of the Xidatan rock series, East Kunlun Mountain. *Sci. China* **2002**, *45*, 20–27. [CrossRef]
33. Liu, Y.; Zhang, R.Q.; Zhang, Z.Y.; Shi, G.H.; Zhang, Q.C.; Abuduwayiti, M.; Liu, J.H. Mineral inclusions and SHRIMP U–Pb dating of zircons from the Alamas nephrite and granodiorite: implications for the genesis of a magnesian skarn deposit. *Lithos* **2015**, *212–215*, 128–144. [CrossRef]
34. Liu, Y.S.; Gao, S.; Hu, Z.C.; Gao, C.G.; Zong, K.Q.; Wang, D.B. Continental and oceanic crust recycling-induced melt–peridotite interactions in the Trans-North China Orogen: U–Pb dating, Hf isotopes and trace elements in zircons from mantle xenoliths. *J. Petrol.* **2010**, *51*, 537–571. [CrossRef]
35. Anderson, T. Correction of common lead in U–Pb analyses that do not report ^{204}Pb. *Chem. Geol.* **2002**, *192*, 59–79. [CrossRef]
36. Elhlou, S.; Belousova, E.; Griffin, W.L.; Pearson, N.J.; O' Reilly, S.Y. Trace element and isotopic composition of GJ–red zircon standard by laser ablation. *Geochim. Cosmochim. Acta* **2006**, *70*, A158. [CrossRef]
37. Sláma, J.; Kosler, J.; Condon, D.J.; Crowley, J.L.; Gerdes, A.; Hanchar, J.M.; Horstwood, M.S.; Morris, G.A.; Nasdala, L.; Norberg, N.; et al. Plesovice zircon—A new natural reference material for U–Pb and Hf isotopic microanalysis. *Chem. Geol.* **2008**, *249*, 1–35. [CrossRef]
38. Che, X.D.; Wu, F.Y.; Wang, R.C.; Gerdes, A.; Ji, W.Q.; Zhao, Z.H. In situ U–Pb isotopic dating of columbite-tantalite by LA-ICP-MS. *Ore Geol. Rev.* **2015**, *65*, 979–989. [CrossRef]
39. Nier, A.O. A redetermination of the relative abundances of the isotope of carbon, nitro, oxygen, argon and potassium. *Physics* **1950**, *77*, 789–793.
40. Liati, A.; Gebauer, D. Constraining the prograde and retrograde P-T-t path of Eocene HP rocks by SHRIMP dating of different zircon domains: inferred rates of heating, burial, cooling and exhumation for central Rhodope, northern Greece. *Contrib. Mineral. Petrol.* **1999**, *135*, 340–354. [CrossRef]
41. Rubatto, D.; Liati, A.; Gebauer, D. Dating UHP metamorphism. In *Ultra-high Pressure Metamorphism*; Compagnoni, R., Carswell, D.A., Eds.; European Mineralogical Union: Budapest, Hungary, 2003; Volume 5, pp. 341–363.
42. DeWitt, E.D.; Armstrong, R.L.; Sutter, J.F.; Zartman, R.E. U–Th–Pb, Rb–Sr, and Ar–Ar mineral and whole-rock isotopic systematics in a metamorphosed granitic terrane, southeastern California. *Geology* **1984**, *95*, 723–739. [CrossRef]
43. Mezger, K. Geochronology in granulites. In *Granulites and Crustal Evolution*; Vielzeuf, D., Vidal, P., Eds.; Kluwer: Amsterdam, The Netherlands, 1990; pp. 451–470.
44. Lee, J.K.; Williams, I.S.; Ellis, D.J. Pb, U and Th diffusion innatural zircon. *Nature* **1997**, *390*, 159–161. [CrossRef]

45. Dahl, P.S. A crystal–chemical basis for Pb retention and fission–trackannealing systematics in U-bearing minerals, with implications for geochronology. *Earth Planet. Sci. Lett.* **1997**, *150*, 277–290. [CrossRef]
46. McLelland, J.; Hamilton, M.; Selleck, B. Zircon U–Pb geochronology of the Ottawan Orogeny, Adirondack Highlands, New York: Regional and tectonic implications. *Precambrian Res.* **2001**, *109*, 39–72. [CrossRef]
47. Qiao, G.; Zhang, H.; Wu, Y.; Jin, M.; Du, W.; Zhao, X. Petrogenesis of the Dahongliutan monzogranite in western Kunlun: Constraints from SHRIMP zircon U–Pb geochronology and geochemical characteris. *Acta Geol. Sin.* **2015**, *89*, 1180–1194, (In Chinese with English abstract).
48. Yan, Q.H.; Qiu, Z.W.; Wang, H.; Wang, M.; Wei, X.P.; Li, P.; Zhang, R.Q.; Li, C.Y.; Liu, J.P. Age of the Dahongliutan rare metal pegmatite deposit, West Kunlun, Xinjiang (NW China): Constraints from LA–ICP–MS U–Pb dating of columbite-(Fe) and cassiterite. *Ore Geol. Rev.* **2018**, *100*, 561–573. [CrossRef]
49. Zhao, Z.; Du, X.J.; Liang, F.H.; Wu, C.; Liu, X.J. Structure and metamorphism of markam gneiss dome from the eastern Tibetan plateau and its implications for crustal thickening, metamorphism, and exhumation. *Geochem. Geophys. Geosystems* **2018**, *20*, 24–45. [CrossRef]
50. Yue, X.; Guo, J.; Mao, S.; Zhu, Z.; Tan, H. Zircon U–Pb age and geochemistry of the Taiyanghe granitoid in western Sichuan, China and its geological significance. *Bull. Mineral. Petrol. Geochem.* **2018**, *37*, 1142–1151, (In Chinese with English abstract).
51. Fei, G.; Tian, J.; Yang, J.; Gao, J.; Tang, W.; Li, J.; Gu, C. New Zircon U–Pb Age of the Super–Large Lijiagou Spodumene Deposit in Songpan–Ganzê Fold Belt, Eastern Tibet: Implications for Early Jurassic Rare-Metal Polymetallic Event. *Acta Geol. Sin.* **2018**, *92*, 1274–1275. [CrossRef]
52. Harrison, T.M.; Duncan, I.; McDougall, I. Diffusion of Ar in biotite: Temperature, pressure and compositional effects. *Geochim. Cosmochim. Acta* **1985**, *49*, 2461–2468. [CrossRef]
53. Dodson, M.H.; MeClelland-Brown, E. Isotopic and palaeomagnetic evidence for rates of cooling, uplift and erosion. In *The Chronology of Geological Record*; Snelling, N.J., Ed.; Geological Society Memory: London, UK, 1985; pp. 315–325.
54. London, D. Pegmatites. *Spec. Publ. Can. Mineral.* **2008**, *10*, 1–347.
55. Sirbescu, M.; Nabelek, P. Crustal melts below 400 °C. *Geology* **2003**, *31*, 685–688. [CrossRef]
56. Li, J.; Chou, I.M. Homogenization experiments of crystal-rich inclusions in spodumene from Jiajika lithium deposit, China, under elevated external pressures in a hydrothermal diamond-anvil cell. *Geofluids* **2017**, *2017*. [CrossRef]
57. Patiño Douce, A.E.; Harris, N. Experimental constraints on Himalayan Anatexis. *J. Petrol.* **1998**, *39*, 689–710. [CrossRef]
58. Chappell, B.W.; White, A.J. Two contrasting granite types: 25 years later. *J. Geol. Soc. Aust.* **2001**, *48*, 489–499. [CrossRef]
59. Martin, R.F.; De Vito, C. The patterns of enrichment in felsic pegmatites ultimately depend on tectonic setting. *Can. Mineral.* **2005**, *43*, 2027–2048. [CrossRef]
60. Černý, P.; London, D.; Novák, M. Granitic pegmatites as reflections of their sources. *Elements* **2012**, *8*, 289–294. [CrossRef]
61. Park, R.G. The Lewisian terrane model: A review. *J. Geol. Soc.* **2005**, *41*, 105–118. [CrossRef]
62. Goodenough, K.M.; Crowley, Q.G.; Krabbendam, M.; Parry, S.F. New U–Pb age constraints for the Laxford Shear Zone, NW Scotland: Evidence for tectonomagmatic processes associated with the formation of a Palaeoproterozoic supercontinent. *Precambrian Res.* **2013**, *233*, 1–19. [CrossRef]
63. Mason, A.J. The Palaeoproterozoic anatomy of the Lewisian Complex, NW Scotland: Evidence for two 'Laxfordian' tectonothermal cycles. *J. Geol. Soc.* **2015**, *173*, 153–169. [CrossRef]
64. Bea, F.; Pereira, M.D.; Stroh, A. Mineral/leucosome trace-element partitioning in a peraluminous migmatite (a laser ablation-ICP-MS study). *Chem. Geol.* **1994**, *117*, 291–312. [CrossRef]
65. Dasgupta, R.; Hirschmann, M.M.; McDonough, W.F.; Spiegelman, M.; Withers, A.C. Trace element partitioning between garnet lherzolite and carbonatite at 6.6 and 8.6 GPa with applications to the geochemistry of the mantle and of mantle-derived melts. *Chem. Geol.* **2009**, *262*, 57–77. [CrossRef]
66. Kellett, D.A.; Godin, L. Pre-Miocene deformation of the Himalayan superstructure, Hidden valley, central Nepal. *J. Geol. Soc.* **2009**, *166*, 261–275. [CrossRef]
67. Groppo, C.; Rolfo, F.; Indares, A. Partial melting in the Higher Himalayan Crystallines of Eastern Nepal: The effect of decompression and implications for the 'Channel Flow' model. *J. Petrol.* **2012**, *53*, 1057–1088. [CrossRef]

68. Groppo, C.; Rolfo, F.; Mosca, P. The cordierite-bearing anatectic rocks of the Higher Himalayan Crystallines (eastern Nepal): Low-pressure anatexis, meltproductivity, melt loss and the preservation of cordierite. *J. Metamorph. Geol.* **2013**, *31*, 187–204. [CrossRef]
69. Groppo, C.; Rubatto, D.; Rolfo, F.; Lombardo, B. Early Oligocene partial melting in the Main Central Thrust Zone (Arun valley, eastern Nepal Himalaya). *Lithos* **2010**, *118*, 287–301. [CrossRef]
70. Stepanov, A.A.; Mavrogenes, J.; Meffre, S.; Davidson, P. The key role of mica during igneous concentration of tantalum. *Contrib. Mineral. Petrol.* **2014**, *167*, 1–8. [CrossRef]
71. Gaidies, F.; Petley-Ragan, A.; Chakraborty, S.; Dasgupta, S.; Jones, P. Constraining the conditions of Barrovian metamorphism in Sikkim, India: P–T–t paths of garnet crystallization in the Lesser Himalayan Belt. *J. Metamorph. Geol.* **2015**, *33*, 23–44. [CrossRef]
72. Shaw, R.A.; Goodenough, K.M.; Roberts, N.M.; Horstwood, M.S.; Chenery, S.R.; Gunn, A.G. Petrogenesis of rare-metal pegmatites in high-grade metamorphic terranes: A case study from the Lewisian Gneiss Complex of north-west Scotland. *Precambrian Res.* **2016**, *281*, 338–362. [CrossRef]
73. Zhang, Z.; Dong, X.; Ding, H.; Tian, Z.; Xiang, H. Metamorphism and partial melting of the Himalayan orogen. *Acta Petrol. Sin.* **2017**, *33*, 2313–2341, (In Chinese with English abstract).
74. Breaks, F.W.; Moore, J.M., Jr. The Ghost Lake batholith, Superior Province of northwestern Ontario: A fertile, S-type, peraluminous granite-rare-element pegmatite system. *Can. Mineral.* **1992**, *30*, 835–876.
75. Partington, G.A.; Mcnaughton, N.J.; Williams, I.S. A review of the geology, mineralization, and geochronology of the greenbushes pegmatite, western Australia. *Econ. Geol.* **1995**, *90*, 616–635. [CrossRef]
76. Morteani, G.; Preinfalk, C.; Horn, A.H. Classification and mineralization potential of the pegmatites of the eastern Brazilian pegmatite province. *Miner. Depos.* **2000**, *35*, 638–655. [CrossRef]
77. Dilek, Y.; Furnes, H. Ophiolite genesis and global tectonics: Geochemical and tectonic fingerprinting of ancient oceanic lithosphere. *GSA Bull.* **2011**, *123*, 387–411. [CrossRef]
78. Xu, Z.Q.; Yang, J.S.; Li, H.B.; Zhang, J.X.; Wu, C.L. *Orogenic Plateau: Terrane Amalgamation, Collision and Uplift in the Qinghai Tibet Plateau*; Geological Publishing House: Beijing, China, 2007; pp. 1–458, (In Chinese with English abstract).
79. Xu, Z.Q.; Yang, J.S.; Li, H.Q.; Wang, R.R.; Cai, Z.H. Indosinian collision-orogenic system of Chinese continent and its orogenic mechanism. *Acta Petrol. Sin.* **2012**, *28*, 1697–1709, (In Chinese with English abstract).
80. Liu, Y.; Deng, J.; Li, C.F.; Shi, G.H.; Zheng, A.L. REE composition in scheelite and scheelite Sm-Nd dating for the Xuebaoding W-Sn-Be deposit in Sichuan. *Chin. Sci. Bull.* **2007**, *52*, 2543–2550. [CrossRef]
81. Xu, Z.Q.; Hou, L.W.; Wang, Z.X.; Fu, X.F.; Hung, M.H. *The Orogenic Process of Songpan-Ganzê Orogenic Zone*; Geological Publishing House: Beijing, China, 1992; p. 190. (In Chinese)
82. Molnar, P.; England, P. Temperatures, heat flux, and frictional stress near major thrust faults. *J. Geophys. Res. Solid Earth* **1990**, *95*, 4833–4856. [CrossRef]
83. Gilder, S.A.; Leloup, P.H.; Courtillot, V. Tectonic evolution of Tancheng–Lujiang (Tan-Lu) Fault via Middle Triassic to Early Cenozoic paleomagnetic data. *J. Geophys. Res. Atmos.* **1999**, *104*, 365–375. [CrossRef]